CHAPTER 5

RESULTS AND DISCUSSION

Effect of Pore Structure on Flow Characteristics Through Pressure Measurement.

Flow characteristics of rarefied gas through a porous material with irregular fine pore shapes largely depend upon the pore structure. Especially, at reduced pressure, the mean free path of the gas molecules becomes longer, so flow resistance, as exemplified by pressure drop across the material, is expected to depend upon the pore structure for an identical flow condition. This is because, some gas molecules may have difficulty entering and moving through some pores of certain size and shape. Fortunately, the complexity of pore structure can be evaluated by adopting the concept of fractal geometry, whose fractal dimension is determined by changing the scale (similarity ratio) and counting the number of relevant elements within the grids. Therefore, combining these two different characteristics, the structural complexity of porous materials can be evaluated both via pressure drop measurement and image analysis.

In this study, the characteristics of rarefied air flow through porous ceramic materials, such as the mean free path, absolute total pressure and pressure drop across the specimens were investigated using the experimental apparatus mentioned in chapter 4. Concurrently, fractal characteristics of the porous ceramic materials, such as the fractal dimension of pore structure, individual and total internal surface area of the pore structure were analyzed visually using fractal counting technique and image analysis. Finally the relationships between air through flow and fractal characteristics of the porous materials were correlated.

1. Relationship between Pressure Drop per Unit Length, Air Flow Rate, Mean Free Path and Absolute Pressure.

Figures 5.1-5.4 and tables 5.1-5.3 show the empirical correlation between pressure drop per unit refractory thickness and absolute total pressure at various mass flow rates. For comparison the calculated values from equation (3.31) are also shown (an example of calculation of calculated pressure drop is shown in appendix 2). As seen

from the figures, pressure drop increases as mass flow rate increases and absolute total pressure decreases, i.e., as the degree of vacuum increases, for each specimen. It is note-worthy that the experimental pressure drop is always higher than the corresponding calculated value and the relative discrepancy between them increases as absolute pressure decreases.

Figures 5.5-5.8 and tables 5.4-5.5 show the plots of measured pressure drop per unit length versus air flow rate with the mean free path as parameter. It clearly shows that pressure drop per unit length increases as air flow rate increases and the effect is higher at longer mean free path. This means that flow resistance for a given mean free path should increase as the pore structure changes or pore size decreases, which is also evident when comparing these figures. Therefore, effective surface area S_V and porosity ε of the specimen are considered to decrease at reduced gas pressure.

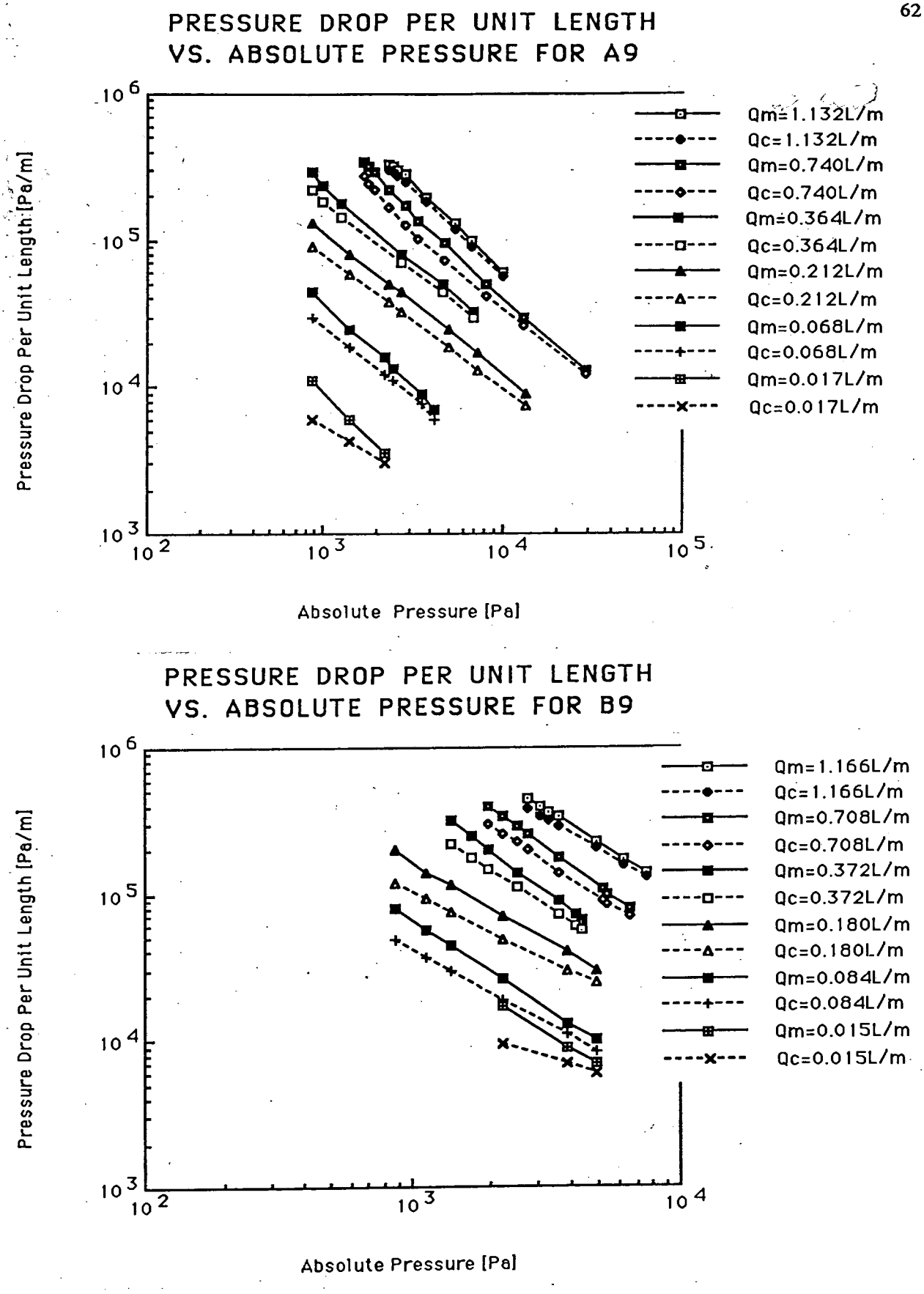

Figure 5.1 Pressure Drop Per Unit Length vs. Absolute Pressure for Specimens A and B

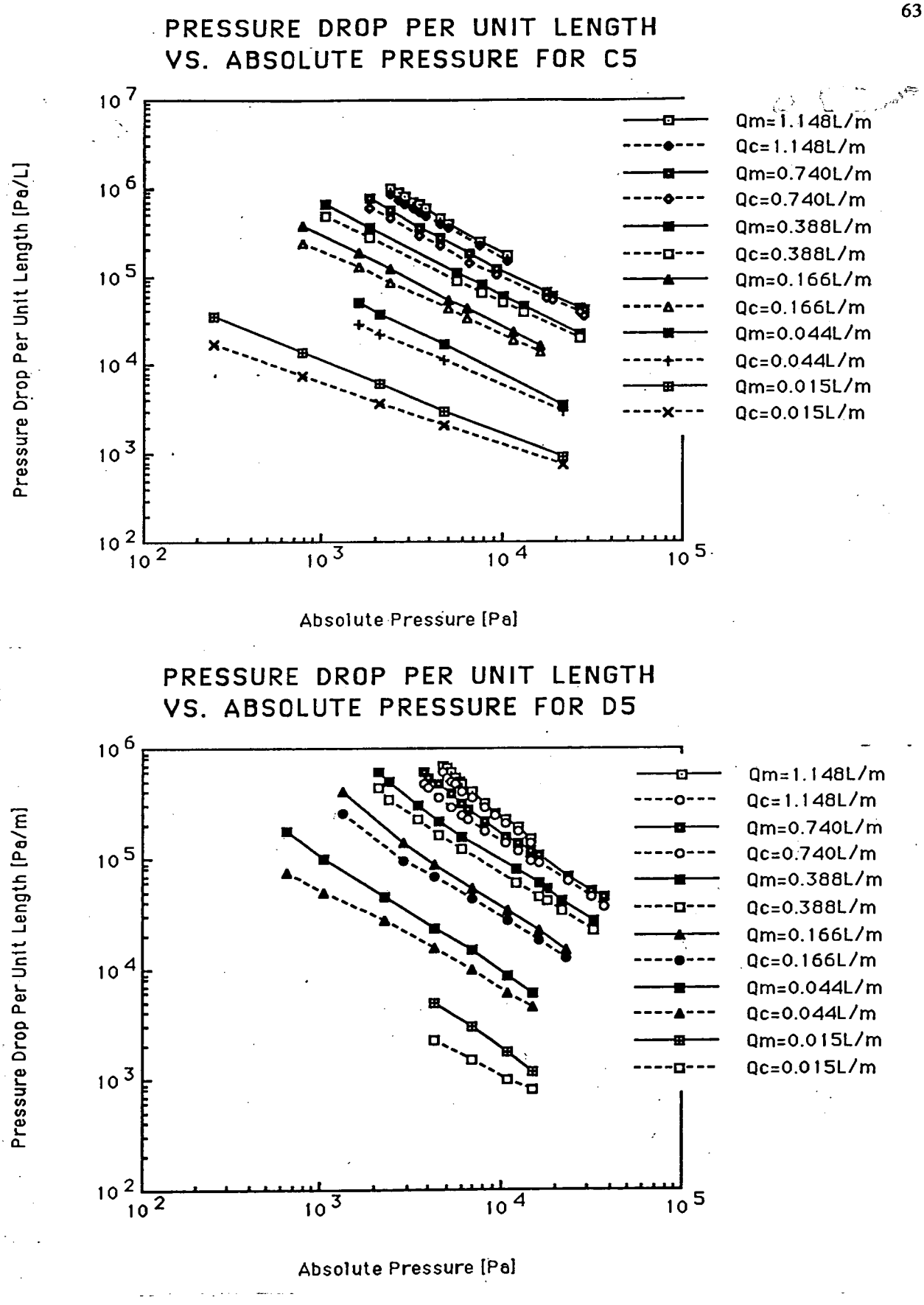

Figure 5.2 Pressure Drop Per Unit Length vs. Absolute Pressure for Specimens C and D

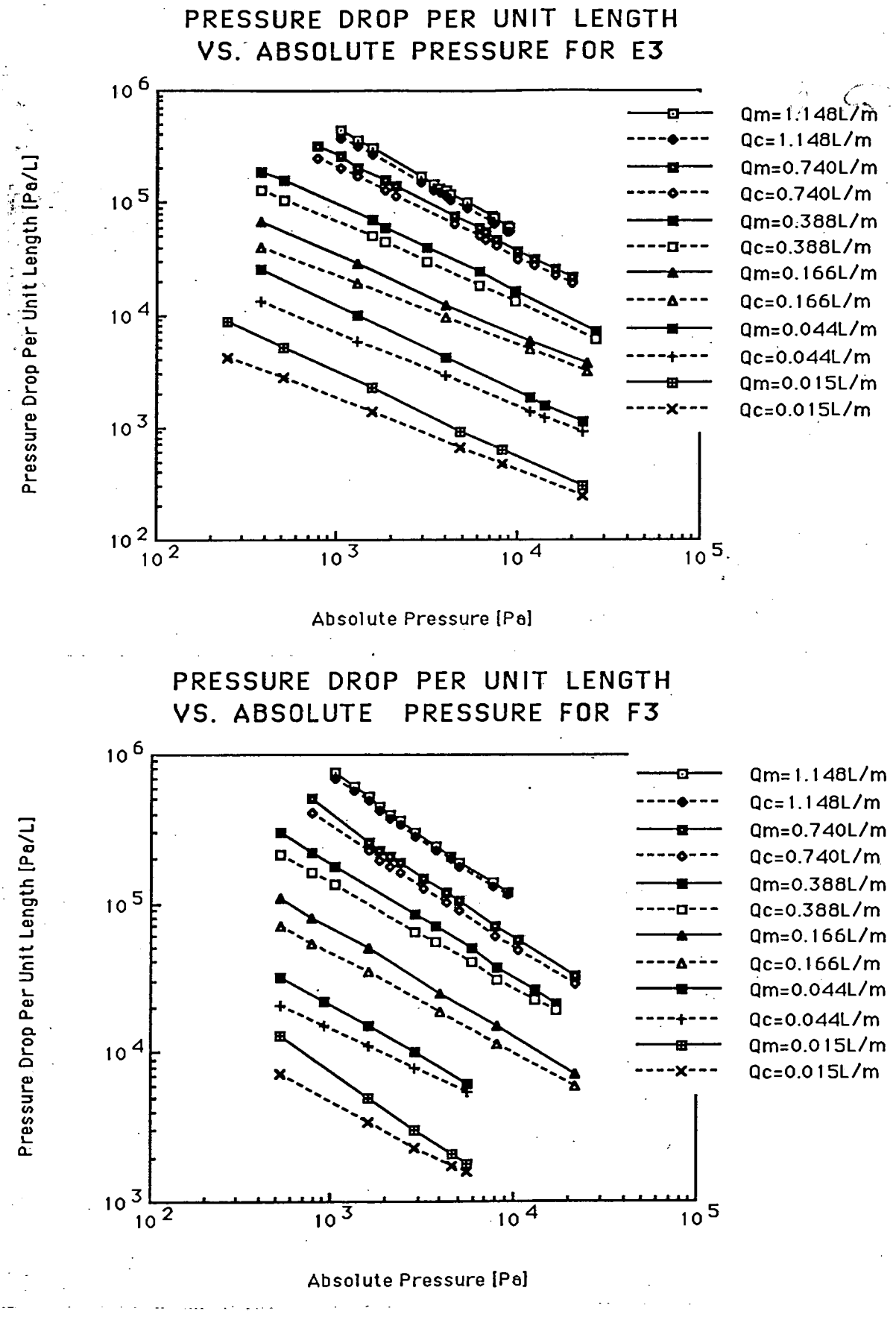

Figure 5.3 Pressure Drop Per Unit Length vs. Absolute Pressure for Specimens E and F

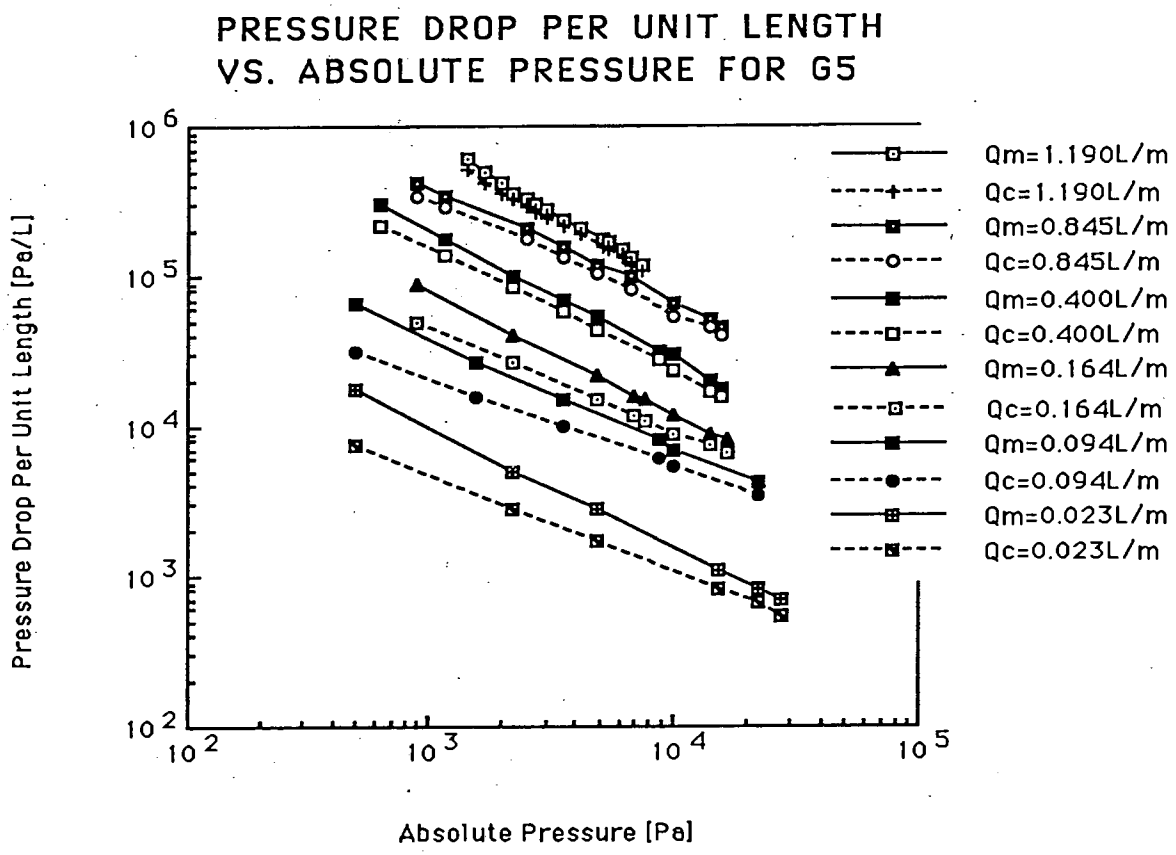

Figure 5.4 Pressure Drop Per Unit Length vs. Absolute Pressure for Specimens G

Table 5.1 Pressure Drop Per Unit Length vs. Absolute Pressure for Specimens A, B and C

Specimen A			Specimen B			Specimen C		
bs P, Pa	DPm/m	DPc/m	Abs P, Pa	DPm/m	DPc/m	Abs P, Pa	DPm/m	DPc/m
2336.5737	3.30e+5	3.00e+5	2336.5737	3.30e+5	3.00e+5	2383.2252	1.00e+6	8.50e+5
2469.8637	3.20e+5	2.90e+5	2469.8637	3.20e+5	2.90e+5	2649.8052	8.80e+5	7.40e+5
2603.1537	3.05e+5	2.75e+5	2603.1537	3.05e+5	2.75e+5	2916.3852	8.00e+5	6.70e+5
2869.7337	2.80e+5	2.50e+5	2869.7337	2.80e+5	2.50e+5	3182.9652	7.00e+5	6.00e+5
3802.7637	1.98e+5	1.82e+5	3802.7637	1.98e+5	1.82e+5	3449.5452	6.50e+5	5.40e+5
5402.2437	1.30e+5	1.18e+5	5402.2437	1.30e+5	1.18e+5	3716.1252	5.80e+5	4.90e+5
6735.1437	1.00e+5	8.90e+4	6735.1437	1.00e+5	8.90e+4	4515.8652	4.50e+5	4.00e+5
0200.6837	6.00e+4	5.72e+4	10200.6837	6.00e+4	5.72e+4	5049.0252	4.00e+5	3.50e+5
670.1237	3.40e+5	2.70e+5	1670.1237	3.40e+5	2.70e+5	7448.2452	2.50e+5	2.24e+5
803.4137	3.20e+5	2.40e+5	1803.4137	3.20e+5	2.40e+5	10647.2052	1.70e+5	1.49e+5
936.7037	2.90e+5	2.20e+5	1936.7037	2.90e+5	2.20e+5	1850.0652	7.75e+5	6.00e+5
2336.5737	2.20e+5	1.65e+5	2336.5737	2.20e+5	1.65e+5	2383.2252	5.60e+5	4.50e+5
2869.7337	1.70e+5	1.28e+5	2869.7337	1.70e+5	1.28e+5	3449.5452	3.60e+5	2.90e+5
3402.8937	1.35e+5	1.03e+5	3402.8937	1.35e+5	1.03e+5	4515.8652	2.70e+5	2.23e+5
4735.7937	9.50e+4	7.22e+4	4735.7937	9.50e+4	7.22e+4	6648.5052	1.80e+5	1.44e+5
8201.3337	5.00e+4	4.20e+4	8201.3337	5.00e+4	4.20e+4	9314.3052	1.20e+5	1.03e+5
3133.0637	3.00e+4	2.65e+4	13133.0637	3.00e+4	2.65e+4	17578.2852	6.50e+4	5.60e+4
9527.7337	1.30e+4	1.21e+4	29527.7337	1.30e+4	1.21e+4	18911.1852	6.00e+4	5.20e+4
870.3837	2.90e+5	2.20e+5	870.3837	2.90e+5	2.20e+5	26908.5852	4.30e+4	3.80e+4
003.6737	2.35e+5	1.85e+5	1003.6737	2.35e+5	1.85e+5	28774.6452	4.00e+4	3.50e+4
270.2537	1.80e+5	1.45e+5	1270.2537	1.80e+5	1.45e+5	1050.3252	6.50e+5	4.80e+5
2736.4437	8.00e+4	7.00e+4	2736.4437	8.00e+4	7.00e+4	1850.0652	3.50e+5	2.69e+5
4602.5037	5.00e+4	4.40e+4	4602.5037	5.00e+4	4.40e+4	5582.1852	1.10e+5	8.63e+4
7001.7237	3.30e+4	3.00e+4	7001.7237	3.30e+4	3.00e+4	7714.8252	8.00e+4	6.38e+4
870.3837	1.30e+5	9.00e+4	870.3837	1.30e+5	9.00e+4	10114.0452	6.00e+4	4.95e+4
403.5437	8.00e+4	5.90e+4	1403.5437	8.00e+4	5.90e+4	13313.0052	4.60e+4	3.81e+4
2336.5737	5.00e+4	3.80e+4	2336.5737	5.00e+4	3.80e+4	26908.5852	2.20e+4	1.94e+4
2736.4437	4.50e+4	3.30e+4	2736.4437	4.50e+4	3.30e+4	783.7452	3.70e+5	2.37e+5
5002.3737	2.50e+4	1.89e+4	5002.3737	2.50e+4	1.89e+4	1583.4852	1.80e+5	1.24e+5
7401.5937	1.70e+4	1.31e+4	7401.5937	1.70e+4	1.31e+4	2383.2252	1.20e+5	8.50e+4
3532.9337	9.00e+3	7.54e+3	13532.9337	9.00e+3	7.54e+3	5049.0252	5.30e+4	4.20e+4
870.3837	4.50e+4	3.00e+4	870.3837	4.50e+4	3.00e+4	6381.9252	4.20e+4	3.30e+4
403.5437	2.50e+4	1.90e+4	1403.5437	2.50e+4	1.90e+4	11446.9452	2.30e+4	1.90e+4
2203.2837	1.60e+4	1.23e+4	2203.2837	1.60e+4	1.23e+4	16245.3852	1.60e+4	1.40e+4
2469.8637	1.35e+4	1.12e+4	2469.8637	1.35e+4	1.12e+4	1583.4852	5.00e+4	2.84e+4
3536.1837	9.00e+3	7.57e+3	3536.1837	9.00e+3	7.57e+3	2116.6452	3.75e+4	2.25e+4
4202.6337	7.00e+3	6.00e+3	4202.6337	7.00e+3	6.00e+3	4782.4452	1.70e+4	1.12e+4
870.3837	1.10e+4	6.01e+3	870.3837	1.10e+4	6.01e+3	21576.9852	3.50e+3	3.00e+3
403.5437	6.00e+3	4.29e+3	1403.5437	6.00e+3	4.29e+3	250.5852	3.50e+4	1.69e+4
2203.2837	3.50e+3	3.02e+3	2203.2837	3.50e+3	3.02e+3	783.7452	1.40e+4	7.40e+3
						2116.6452	6.00e+3	3.70e+3
						4782.4452	3.00e+3	2.10e+3
						21576.9852	9.26e+2	7.60e+2

Table 5.2 Pressure Drop Per Unit Length vs. Absolute Pressure for Specimens D and E

Specimen D			Specimen E		
Abs P, Pa	DPm/m	DP/m	Abs P, Pa	DPm/m	DPc/m
4782.4452	7.00e+5	6.02e+5	1050.3252	4.50e+5	3.80e+5
5049.0252	6.50e+5	5.50e+5	1316.9052	3.60e+5	3.15e+5
5315.6052	6.00e+5	5.05e+5	1583.4852	3.00e+5	2.70e+5
5582.1852	5.50e+5	4.68e+5	2916.3852	1.70e+5	1.53e+5
5848.7652	5.00e+5	4.26e+5	3449.5452	1.45e+5	1.31e+5
6115.3452	4.70e+5	3.99e+5	3716.1252	1.35e+5	1.23e+5
6915.0852	4.00e+5	3.50e+5	3982.7052	1.27e+5	1.15e+5
8247.9852	3.10e+5	2.88e+5	4249.2852	1.20e+5	1.06e+5
9314.3052	2.60e+5	2.44e+5	5315.6052	1.00e+5	8.91e+4
10647.2052	2.30e+5	2.11e+5	7181.6652	7.50e+4	6.66e+4
12513.2652	1.95e+5	1.77e+5	7448.2452	7.20e+4	6.45e+4
14645.9052	1.50e+5	1.40e+5	8781.1452	6.20e+4	5.57e+4
3716.1252	6.00e+5	4.85e+5	9047.7252	6.00e+4	5.40e+4
3982.7052	5.50e+5	4.33e+5	783.7452	3.20e+5	2.46e+5
4515.8652	4.80e+5	3.63e+5	1050.3252	2.60e+5	2.03e+5
5315.6052	3.90e+5	2.95e+5	1316.9052	2.05e+5	1.71e+5
6115.3452	3.20e+5	2.49e+5	1850.0652	1.60e+5	1.30e+5
6648.5052	2.80e+5	2.26e+5	2116.6452	1.40e+5	1.15e+5
8247.9852	2.20e+5	1.81e+5	4515.8652	7.50e+4	6.50e+4
10647.2052	1.60e+5	1.41e+5	6115.3452	6.00e+4	5.00e+4
12513.2652	1.40e+5	1.19e+5	6648.5052	5.50e+4	4.60e+4
14645.9052	1.20e+5	9.56e+4	7714.8252	4.70e+4	4.10e+4
16245.3852	1.10e+5	9.09e+4	10114.0452	3.70e+4	3.10e+4
23709.6252	7.00e+4	6.24e+4	12513.2652	3.10e+4	2.70e+4
31973.6052	5.20e+4	4.61e+4	16245.3852	2.50e+4	2.20e+4
37571.7852	4.50e+4	3.70e+4	20244.0852	2.15e+4	1.90e+4
2116.6452	6.00e+5	4.31e+5	383.8752	1.90e+5	1.30e+5
2383.2252	5.00e+5	3.48e+5	517.1652	1.60e+5	1.05e+5
3449.5452	3.00e+5	2.25e+5	1583.4852	7.00e+4	5.00e+4
4515.8652	2.20e+5	1.65e+5	1850.0652	6.00e+4	4.50e+4
6115.3452	1.60e+5	1.24e+5	3182.9652	4.00e+4	3.00e+4
12246.6852	8.00e+4	6.14e+4	6115.3452	2.40e+4	1.80e+4
16245.3852	6.00e+4	4.64e+4	9847.4652	1.60e+4	1.30e+4
18111.4452	5.30e+4	4.16e+4	26908.5852	7.00e+3	6.00e+3
21576.9852	4.30e+4	3.29e+4	383.8752	6.80e+4	3.94e+4
32240.1852	2.80e+4	2.30e+4	1316.9052	2.80e+4	1.90e+4
1316.9052	4.00e+5	2.54e+5	3982.7052	1.20e+4	9.50e+3
2916.3852	1.40e+5	9.76e+4	11713.5252	5.80e+3	4.80e+3
4249.2852	9.00e+4	6.84e+4	24242.7852	3.60e+3	3.10e+3
6915.0852	5.50e+4	4.34e+4	383.8752	2.50e+4	1.30e+4
10913.7852	3.50e+4	2.79e+4	1316.9052	1.00e+4	5.80e+3
16245.3852	2.30e+4	1.86e+4	3982.7052	4.20e+3	2.90e+3
22909.8852	1.50e+4	1.30e+4	11713.5252	1.85e+3	1.40e+3
650.4552	1.80e+5	7.62e+4	14242.7852	1.55e+3	1.20e+3
1050.3252	1.01e+5	5.07e+4	22909.8852	1.10e+3	9.00e+2
2249.9352	4.50e+4	2.77e+4	250.5852	8.50e+3	4.20e+3
4249.2852	2.40e+4	1.60e+4	517.1652	5.00e+3	2.70e+3
6915.0852	1.50e+4	9.89e+3	1583.4852	2.20e+3	1.35e+3
10913.7852	9.00e+3	6.09e+3	4915.7352	9.20e+2	6.60e+2
14912.4852	6.00e+3	4.50e+3	8247.9852	6.40e+2	4.80e+2
4249.28	5.00e+3	2.30e+5	22909.8852	3.00e+2	2.50e+2
6915.08	3.00e+3	1.50e+3			
10913.78	1.80e+3	1.00e+3			
14912.48	1.20e+3	8.00e+2			

Table 5.3 Pressure Drop Per Unit Length vs. Absolute Pressure for Specimens F and G

Specimen F			Specimen G		
Abs P, Pa	DPm/m	DPc/m	Abs P, Pa	DPm/m	DPc/m
1050.3252	7.50e+5	7.00e+5	1423.5372	6.00e+5	5.14e+5
1316.9052	6.20e+5	5.81e+5	1690.1172	5.00e+5	4.24e+5
1583.4852	5.20e+5	4.87e+5	1956.6972	4.20e+5	3.59e+5
1850.0652	4.50e+5	4.22e+5	2223.2772	3.60e+5	3.26e+5
2116.6452	4.00e+5	3.73e+5	2489.8572	3.30e+5	2.96e+5
2383.2252	3.60e+5	3.36e+5	2756.4372	3.00e+5	2.70e+5
2916.3852	3.00e+5	2.80e+5	3023.0172	2.80e+5	2.50e+5
3716.1252	2.45e+5	2.31e+5	3556.1772	2.40e+5	2.17e+5
4515.8652	2.10e+5	1.99e+5	4222.6272	2.10e+5	1.89e+5
5049.0252	1.90e+5	1.80e+5	5155.6572	1.80e+5	1.58e+5
7714.8252	1.40e+5	1.31e+5	5422.2372	1.70e+5	1.48e+5
9314.3052	1.20e+5	1.14e+5	6221.9772	1.50e+5	1.33e+5
783.7452	5.00e+5	4.14e+5	6755.1372	1.32e+5	1.20e+5
1583.4852	2.60e+5	2.25e+5	7554.8772	1.20e+5	1.10e+5
1850.0652	2.30e+5	1.95e+5	890.3772	4.20e+5	3.50e+5
2116.6452	2.10e+5	1.79e+5	1156.9572	3.50e+5	2.90e+5
2383.2252	1.90e+5	1.65e+5	2489.8572	2.10e+5	1.80e+5
3182.9652	1.50e+5	1.25e+5	3556.1772	1.60e+5	1.35e+5
4249.2852	1.20e+5	1.01e+5	4889.0772	1.20e+5	1.05e+5
5049.0252	1.05e+5	9.00e+4	6755.1372	1.00e+5	8.26e+4
7848.1152	7.00e+4	6.00e+4	10220.6772	6.50e+4	5.50e+4
10647.2052	5.60e+4	4.80e+4	14219.3772	5.10e+4	4.50e+4
21576.9852	3.29e+4	2.86e+4	16085.4372	4.50e+4	4.10e+4
517.1652	3.00e+5	2.17e+5	623.7972	3.00e+5	2.20e+5
783.7452	2.20e+5	1.63e+5	1156.9572	1.80e+5	1.40e+5
1050.3252	1.80e+5	1.35e+5	2223.2772	1.00e+5	8.50e+4
2916.3852	8.50e+4	6.50e+4	3556.1772	7.00e+4	5.80e+4
3716.1252	7.00e+4	5.50e+4	4889.0772	5.50e+4	4.40e+4
5848.7652	5.00e+4	4.00e+4	8887.7772	3.20e+4	2.80e+4
8247.9852	3.65e+4	3.10e+4	10220.6772	3.00e+4	2.40e+4
13313.0052	2.60e+4	2.22e+4	14219.3772	2.00e+4	1.70e+4
17311.7052	2.15e+4	1.91e+4	16085.4372	1.80e+4	1.60e+4
517.1652	1.10e+5	7.02e+4	890.3772	9.00e+4	5.01e+4
783.7452	8.00e+4	5.40e+4	2223.2772	4.00e+4	2.70e+4
1583.4852	5.00e+4	3.42e+4	4889.0772	2.20e+4	1.50e+4
3982.7052	2.50e+4	1.85e+4	7021.7172	1.60e+4	1.20e+4
8247.9852	1.50e+4	1.15e+4	7821.4572	1.50e+4	1.10e+4
21576.9852	7.20e+3	5.90e+3	10220.6772	1.20e+4	9.00e+3
517.1652	3.20e+4	2.03e+4	14219.3772	9.00e+3	7.50e+3
917.0352	2.20e+4	1.49e+4	16885.1772	8.00e+3	6.50e+3
1583.4852	1.50e+4	1.10e+4	490.5072	6.50e+4	3.18e+4
2916.3852	1.00e+4	8.00e+3	1556.8272	2.70e+4	1.60e+4
5582.1852	6.20e+3	5.50e+3	3556.1772	1.50e+4	1.00e+4
517.1652	1.30e+4	7.10e+3	8887.7772	8.00e+3	6.00e+3
1583.4852	5.00e+3	3.39e+3	10220.6772	7.00e+3	5.50e+3
2916.3852	3.00e+3	2.32e+3	22216.7772	4.30e+3	3.50e+3
4249.2852	2.08e+3	1.73e+3	490.5072	1.80e+4	7.52e+3
5582.1852	1.80e+3	1.59e+3	2223.2772	5.00e+3	2.80e+3
			4889.0772	2.80e+3	1.70e+3
			15552.2772	1.10e+3	8.00e+2
			22216.7772	8.20e+2	6.50e+2
			27548.3772	7.00e+2	5.50e+2

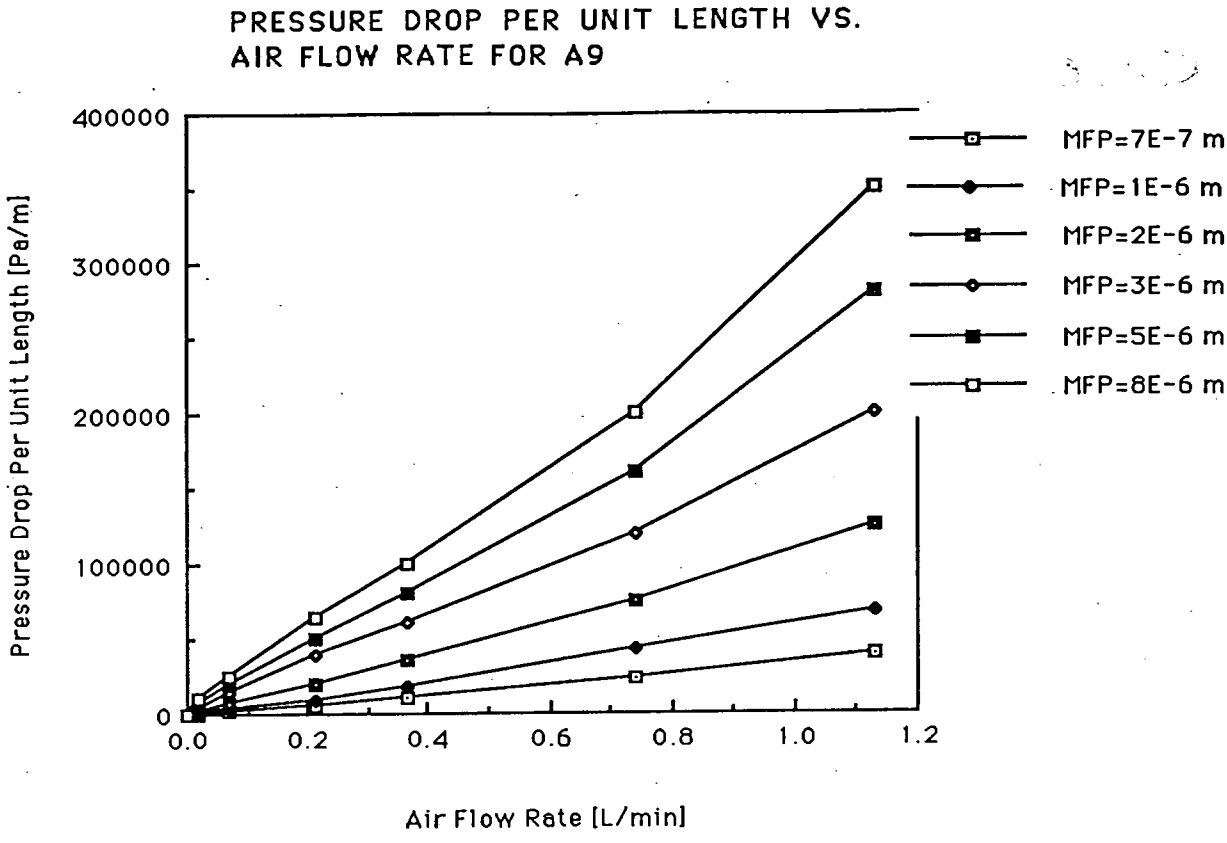

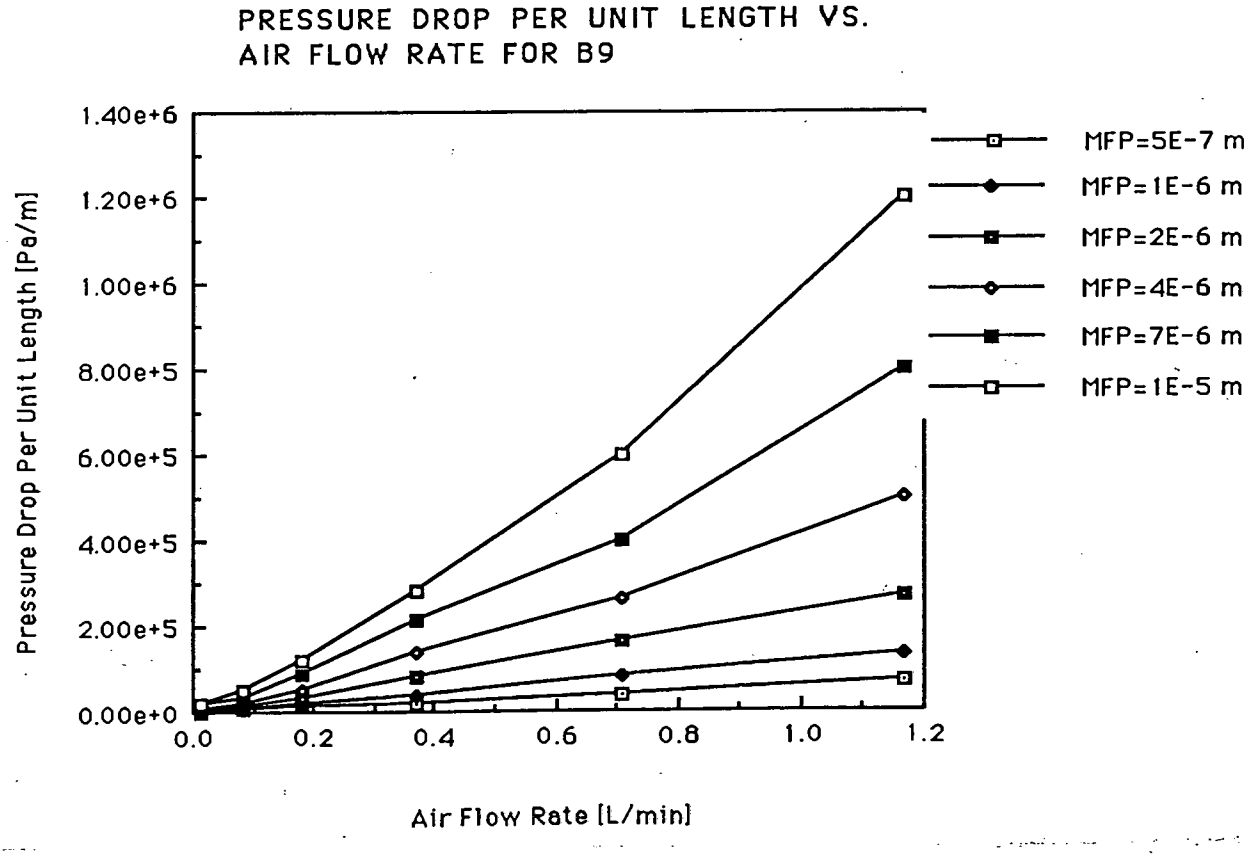

Figure 5.5 Pressure Drop Per Unit Length vs. Mass Flow Rate for Specimens A and B

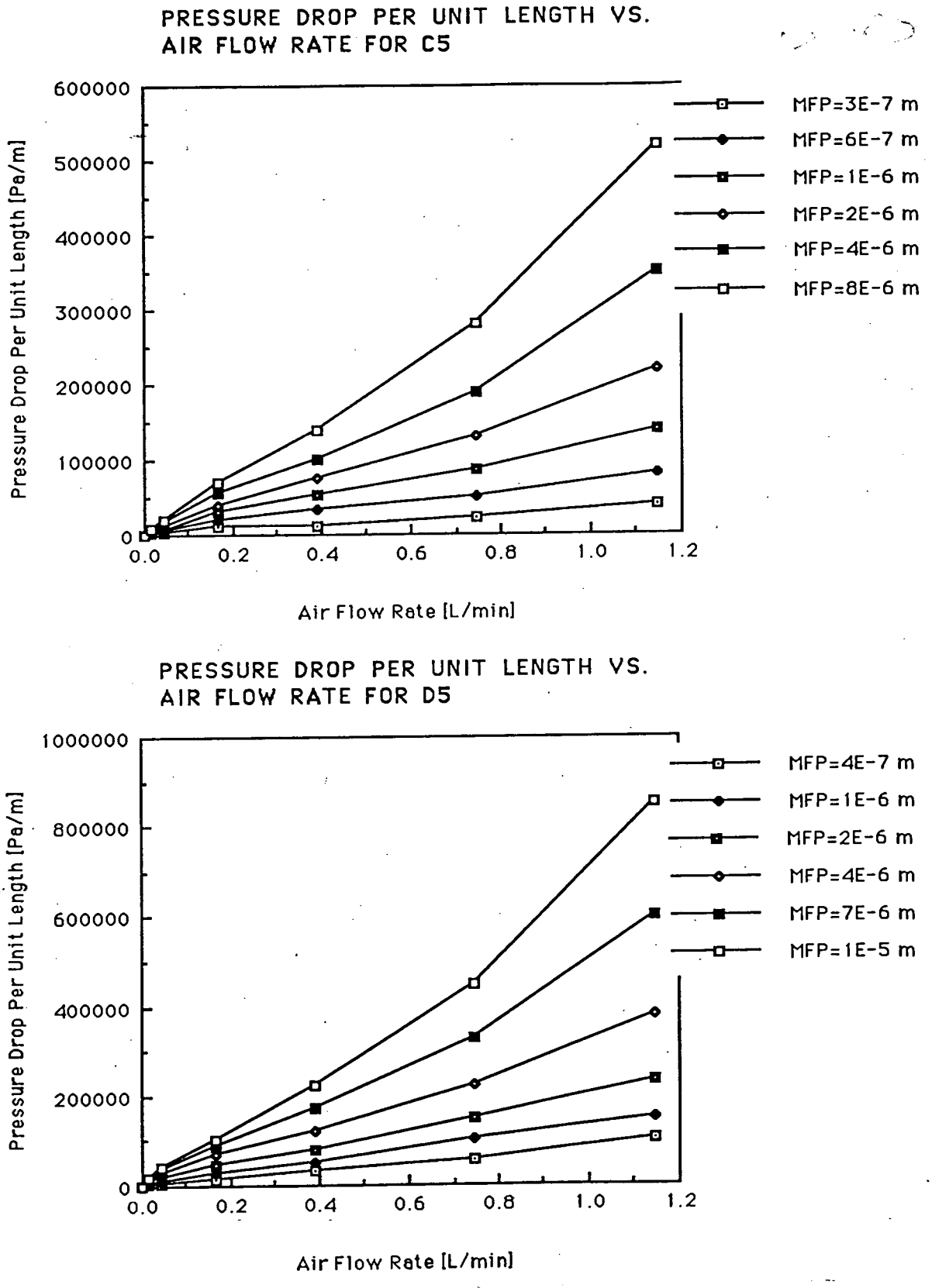

Figure 5.6 Pressure Drop Per Unit Length vs. Mass Flow Rate for Specimens C and D

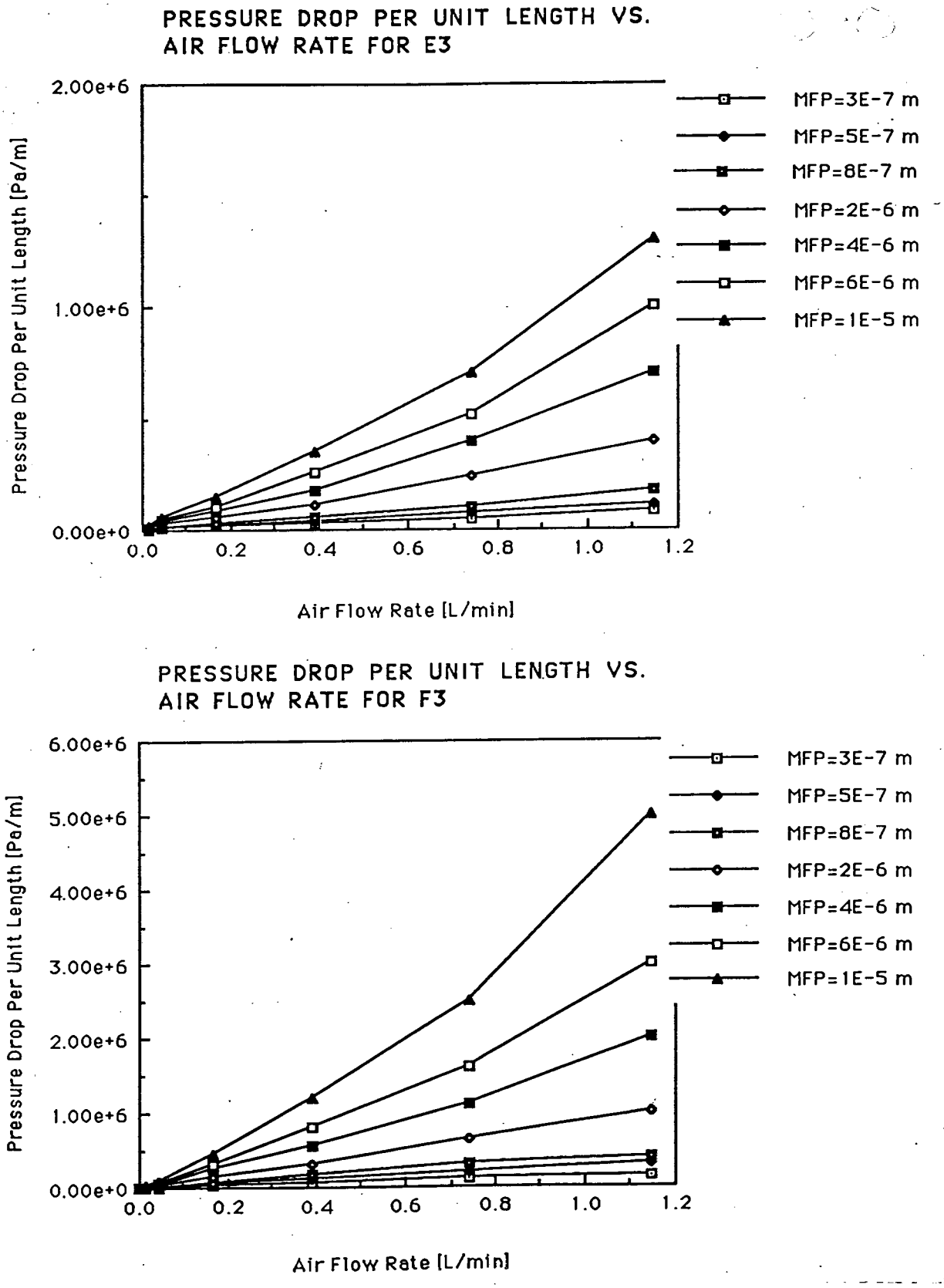

Figure 5.7 Pressure Drop Per Unit Length vs. Mass Flow Rate for Specimens E and F

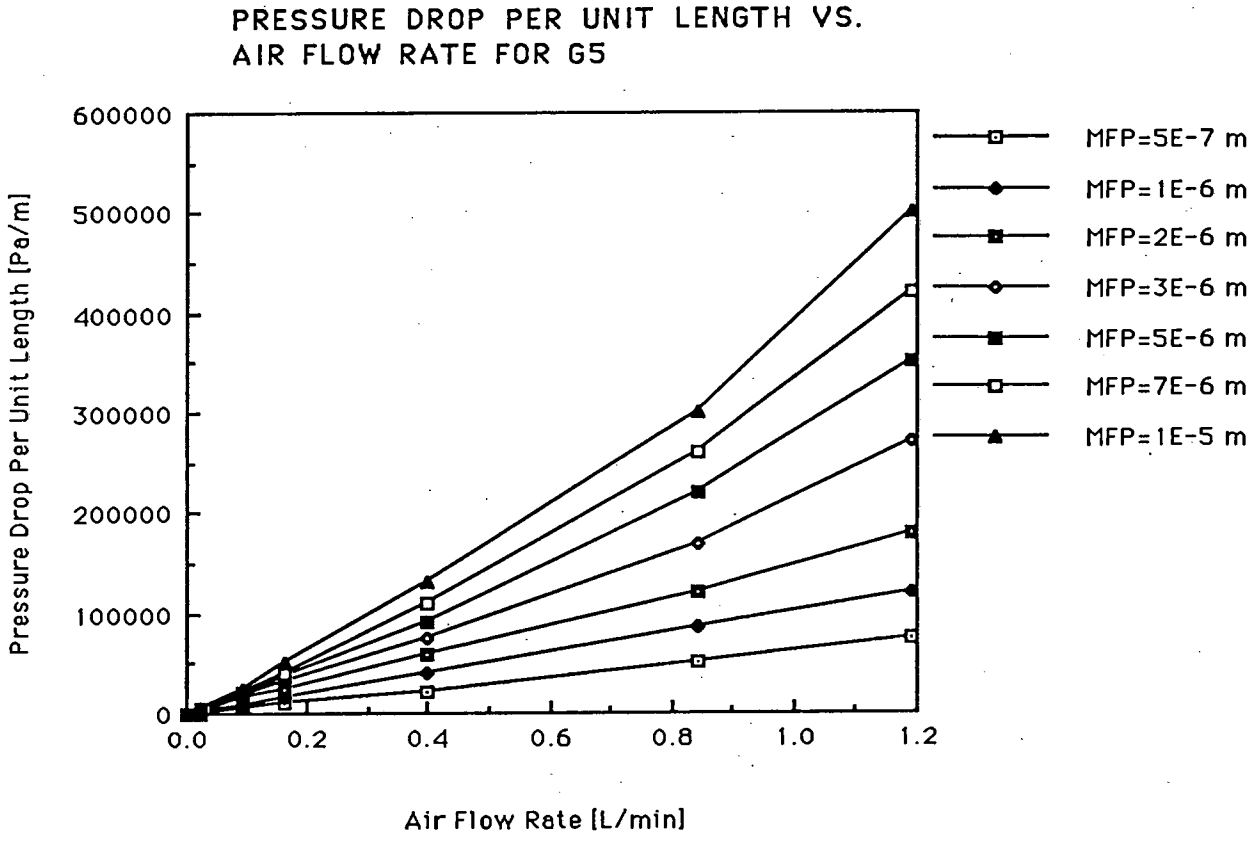

Figure 5.8 Pressure Drop Per Unit Length vs. Mass Flow Rate for Specimen G

Table 5.4 Pressure Drop Per Unit Length vs. Mass Flow Rate for Specimens A, B, C and D

Specimen A

Q, L/min	DP/m MFP= 7*10-7, m	DP/m MFP=1*10-6, m	DP/m MFP= 2*10-6, m	DP/m MFP= 3*10-6, m	DP/m MFP= 5*10-6, m	DP/m MFP=8*10-6, m
1.132	40000	68000	125000	200000	280000	350000
0.740	24000	42000	75000	120000	160000	200000
0.364	10200	18000	35000	75000	80000	100000
0.212	5500	9000	20000	40000	50000	65000
0.068	2000	3000	7000	15000	20000	25000
0.017	700	900	1900	3000	7000	10000
0.000	0	0	0	0	0	0

Specimen B

Q, L/min	DP/m MFP= 5*E-7, m	DP/m MFP=1*E-6, m	DP/m MFP= 2*E-6, m	DP/m MFP= 4*E-6, m	DP/m MFP=7*E-6, m	DP/m MFP=1*E-5, m
1.166	70000	130000	270000	500000	800000	1200000
0.708	40000	80000	160000	260000	400000	600000
0.372	20000	40000	80000	140000	210000	280000
0.180	10000	18000	30000	52000	90000	120000
0.084	4000	7000	13000	21000	33000	50000
0.015	1100	2000	4200	8000	16000	20000
0.000	0	0	0	0	0	0

Specimen C

Q, L/min	DP/m MFP=3*10-7, m	DP/m MFP=6*10-7, m	DP/m MFP=1*10-6, m	DP/m MFP=2*10-6, m	DP/m MFP=4*10-6, m	DP/m MFP=8*10-6, m
1.148	40000	80000	140000	220000	350000	520000
0.746	22000	50000	85000	130000	190000	280000
0.388	12000	32000	52000	75000	100000	140000
0.166	10000	20000	30000	40000	55000	70000
0.044	4000	4800	6000	10000	18000	20000
0.015	1500	1800	2400	3500	5500	7000
0.000	0	0	0	0	0	0

Specimen D

Q, L/min	DP/m MFP=4*10-7, m	DP/m MFP=1*10-6, m	DP/m MFP= 2*10-6, m	DP/m MFP=4*10-6, m	DP/m MFP=7*10-6, m	DP/m MFP=1*10-5, m
1.148	100000	150000	230000	380000	600000	850000
0.746	55000	100000	150000	220000	330000	450000
0.388	32000	50000	80000	120000	170000	220000
0.166	15000	30000	45000	70000	90000	100000
0.044	5000	8000	20000	30000	38000	40000
0.015	2800	3000	12000	12000	13000	17000
0.000	0	0	0	0	0	0

Table 5.5 Pressure Drop Per Unit Length vs. Mass Flow Rate for Specimens E, F and G

Specimen E Q, L/min	DP/m MFP=3*10-7, m	DP/m MFP=5*10-7, m	DP/m MFP=8*10-7, m	DP/m MFP=2*10-6, m	DP/m MFP=4*10-6, m	DP/m MFP=6*10-6, m	DP/m MFP=1*10-5, m
1.148	80000	110000	180000	400000	700000	1000000	1300000
0.740	48000	70000	100000	240000	400000	520000	700000
0.388	30000	40000	60000	110000	180000	260000	350000
0.166	15000	22000	32000	60000	85000	100000	150000
0.044	6000	8500	12000	25000	40000	50000	60000
0.015	1000	1500	2200	5000	9000	11000	14000
0.000	0	0	0	0	0	0	0

Specimen F Q, L/min	DP/m MFP=3*10-7, m	DP/m MFP=5*10-7, m	DP/m MFP=8*10-7, m	DP/m MFP=2*10-6, m	DP/m MFP=4*10-6, m	DP/m MFP=6*10-6, m	DP/m MFP=1*10-5, m
1.148	150000	300000	400000	1000000	2000000	3000000	5000000
0.740	100000	200000	300000	650000	1100000	1600000	2500000
0.388	60000	100000	160000	300000	550000	800000	1200000
0.166	25000	45000	60000	130000	250000	300000	450000
0.044	3500	6000	10000	22000	40000	50000	90000
0.015	1500	2500	4000	7000	10000	12000	16000
0.000	0	0	0	0	0	0	0

Specimen G Q, L/min	DP/m MFP=5*10-7, m	DP/m MFP=1*10-6	DP/m MFP=2*10-6, m	DP/m MFP=3*10-6, m	DP/m MFP=5*10-6, m	DP/m MFP=7*10-6, m	DP/m MFP=1*10-5, m
1.190	75000	120000	180000	270000	350000	420000	500000
0.845	50000	85000	120000	170000	220000	260000	300000
0.400	22000	40000	60000	75000	90000	110000	130000
0.164	10000	15000	25000	31000	38000	40000	50000
0.094	5000	9000	15000	18000	20000	22000	25000
0.023	1200	1800	2800	3800	4100	5000	6000
0.000	0	0	0	0	0	0	0

2. Relationship between Specific Surface Area of Particles, Air Flow Rate and Mean Free Path.

Specific surface area of inter-particle pores was defined as the ratio of the total surface area of particles (m^2) to the total volume of particles (m^3) in a specimen. The specific surface area for each specimen was calculated from equation (3.31) assuming that it is applicable even for rarefied gas flow (an example of calculation of S_V, is shown in appendix 2). Figures 5.9-5.12 show the relationship between specific surface area of inter-particle pore and air flow through the specimen with the mean free path as parameter. At a short mean free path, S_V showed only slight changed with increasing air flow rate. But at a long mean free path, the S_V value dropped remarkably with increasing air flow rate, which seemed to confirm some relationship between the pore structure and flow characteristics of gas through the porous material.

Figures 5.13-5.16 and tables 5.6-5.7 show log-log plots of the specific surface area of particles versus the mean free path λ, with air flow rate as parameter. Although the S_V axis is magnified, the calculated values of S_V obtained at different flow rates for all specimens do not change significantly at the small λ region. But at a large λ, S_V decreased sharply with λ and its slope was steeper at a higher flow rate. The same trend was observed for all specimens despite the fact that pore shapes and sizes were different, and that the sharp drop of S_V started around Kn = 0.01 that corresponds to the slip-flow region. In the large Kn region, gas molecules had difficulty penetrating into small pores and caves because of the longer mean free path of gas molecules. As a result, the gas seemed to flow through a narrower opening as compared to the actual opening even at the same mass flow rate, as shown in figures 5.9-5.12. Table 5.8 shows the calculated value of Kn for each specimen. This change can be interpreted as follows. At small Kn region, a change of the mean free path does not affect flow characteristics so much and thus S_V does not change. But at larger Kn region, more gas molecules tend to flow mainly through larger pores, which results in the effective flow area becoming narrower than the actual pore area. As a result, a gas has to flow through a narrower space as compared to the actual space for large Kn even at the same mass flow rate. Therefore, the effective surface area (as shown in figure 5.17) decreased as the absolute total pressure decreased and the resultant pressure drop became higher than the

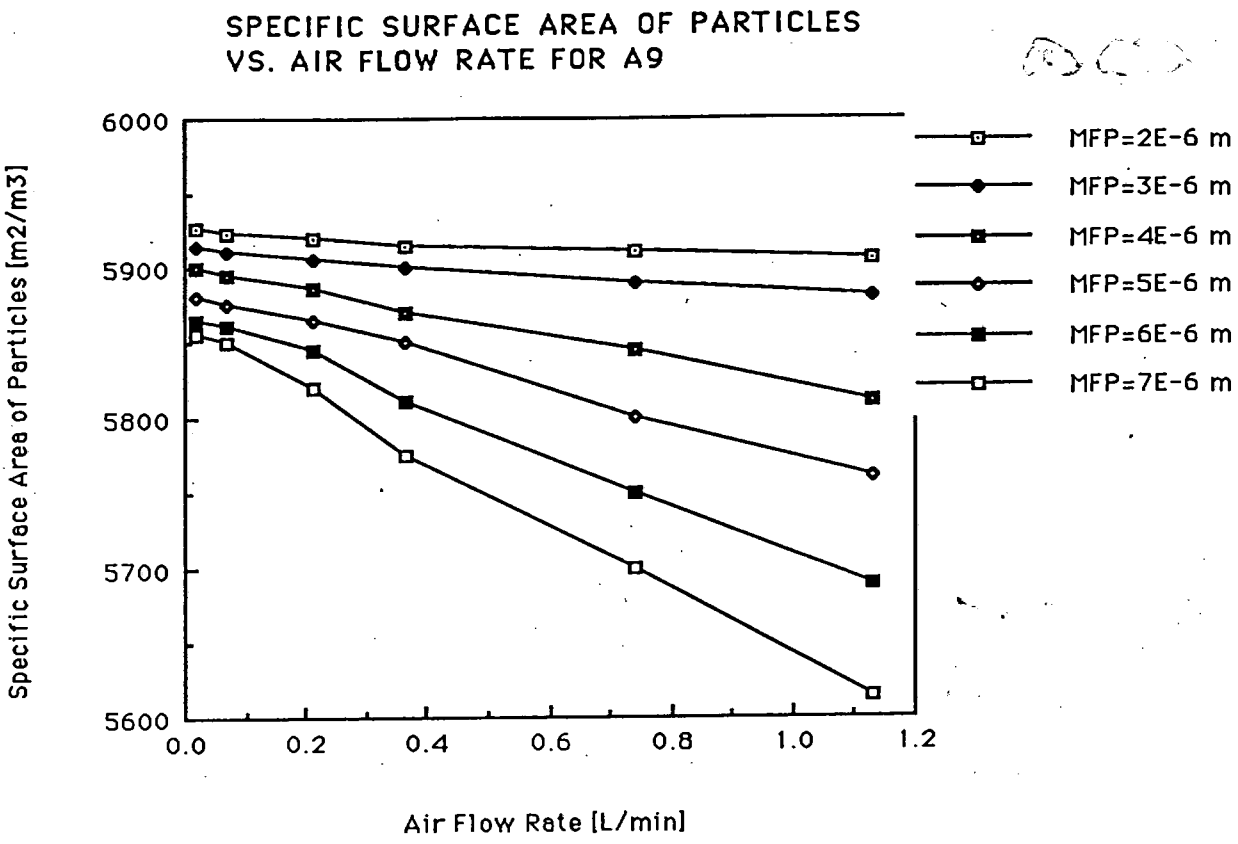

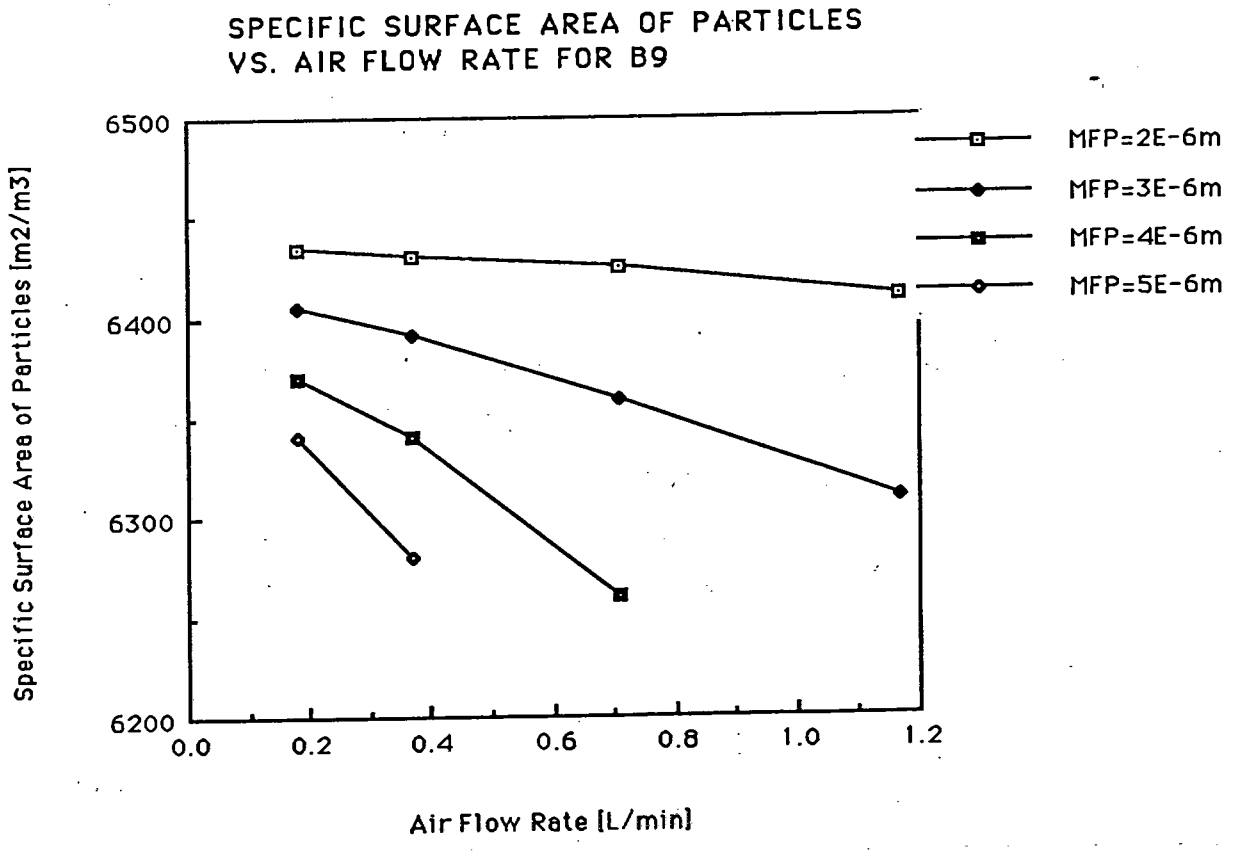

Figure 5.9 Specific Surface Area of Particles vs. Mass Flow Rate for Specimens A and B

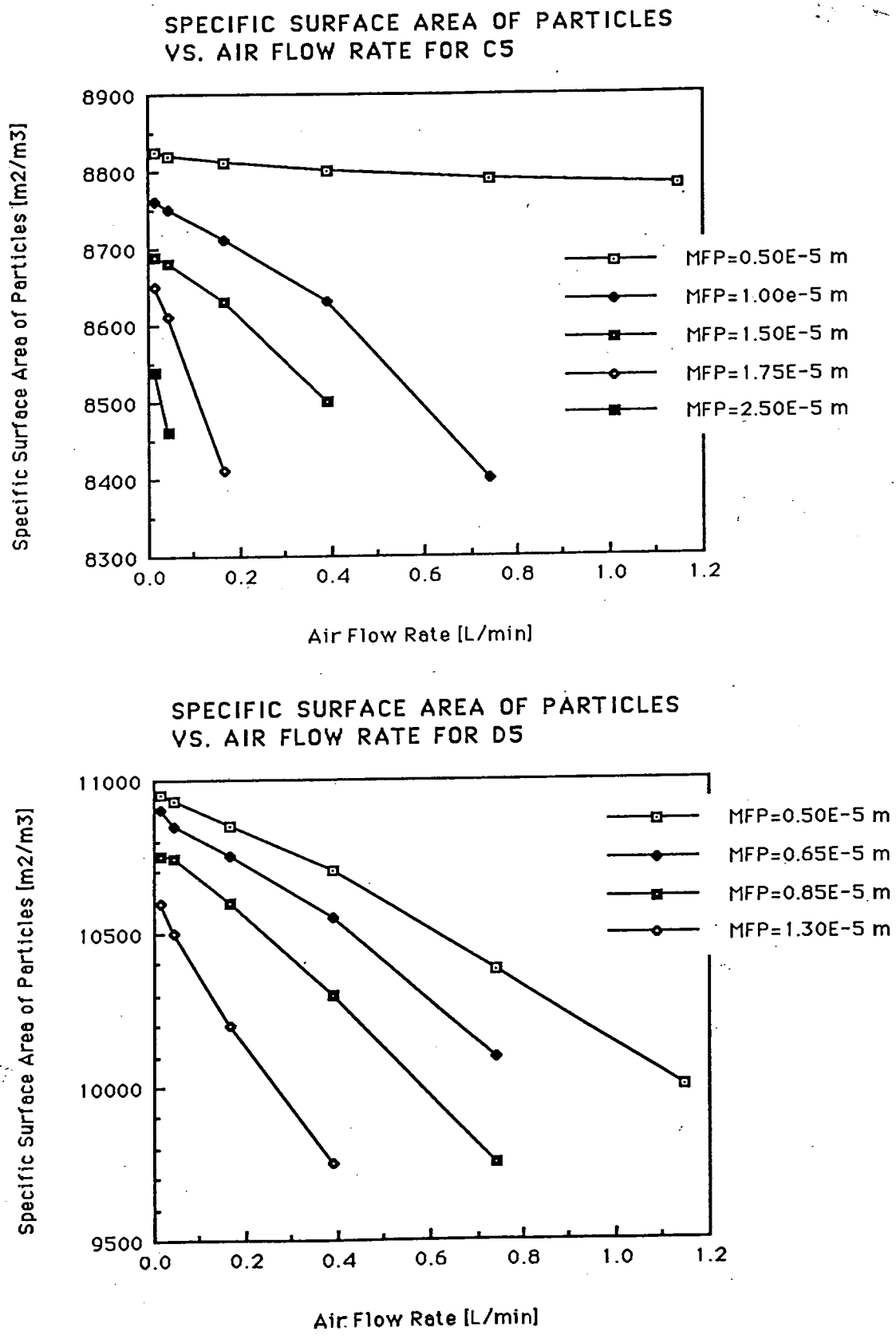

Figure 5.10 Specific Surface Area of Particles vs. Mass Flow Rate for Specimens C and D

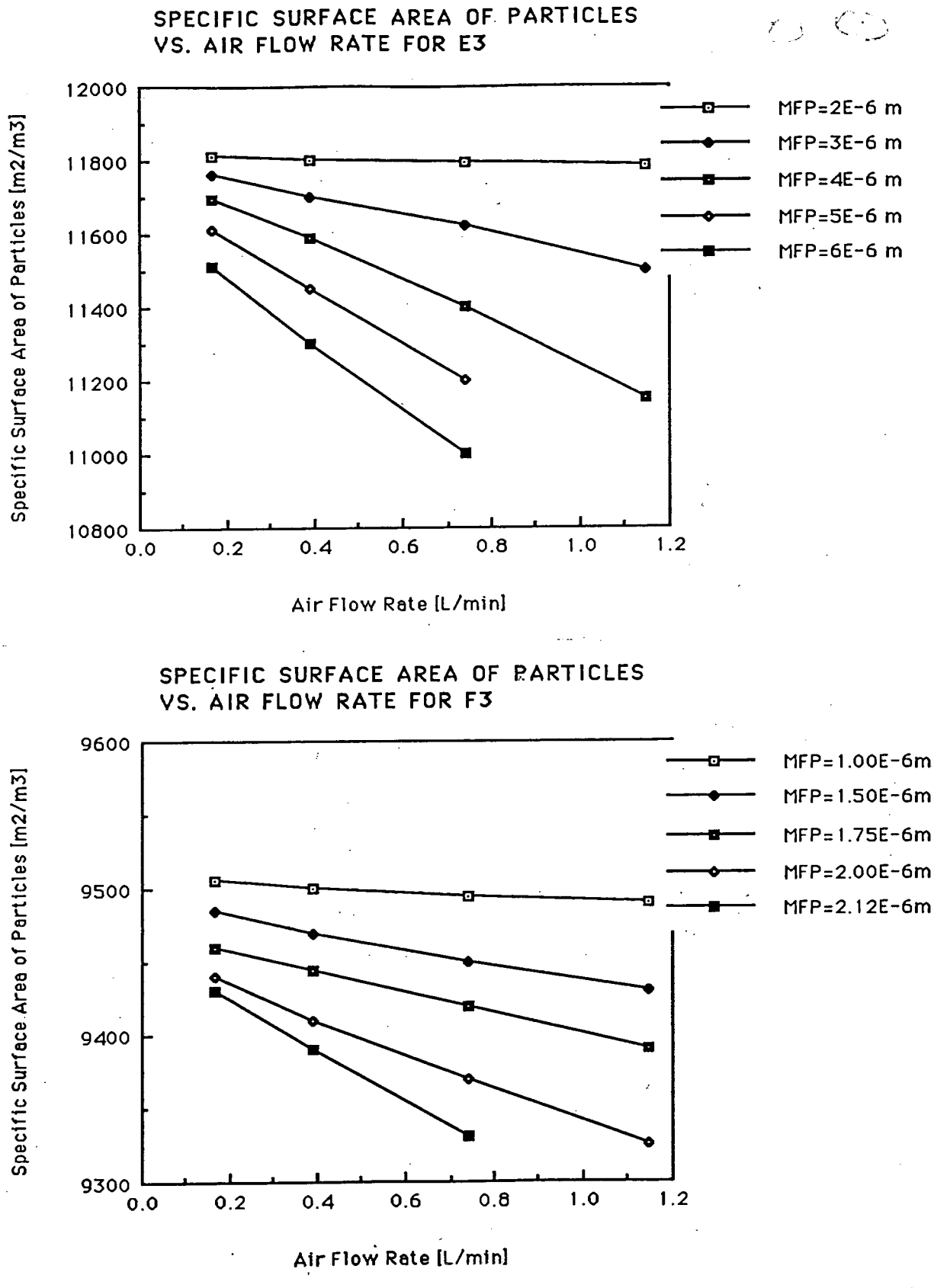

Figure 5.11 Specific Surface Area of Particles vs. Mass Flow Rate for Specimens E and F

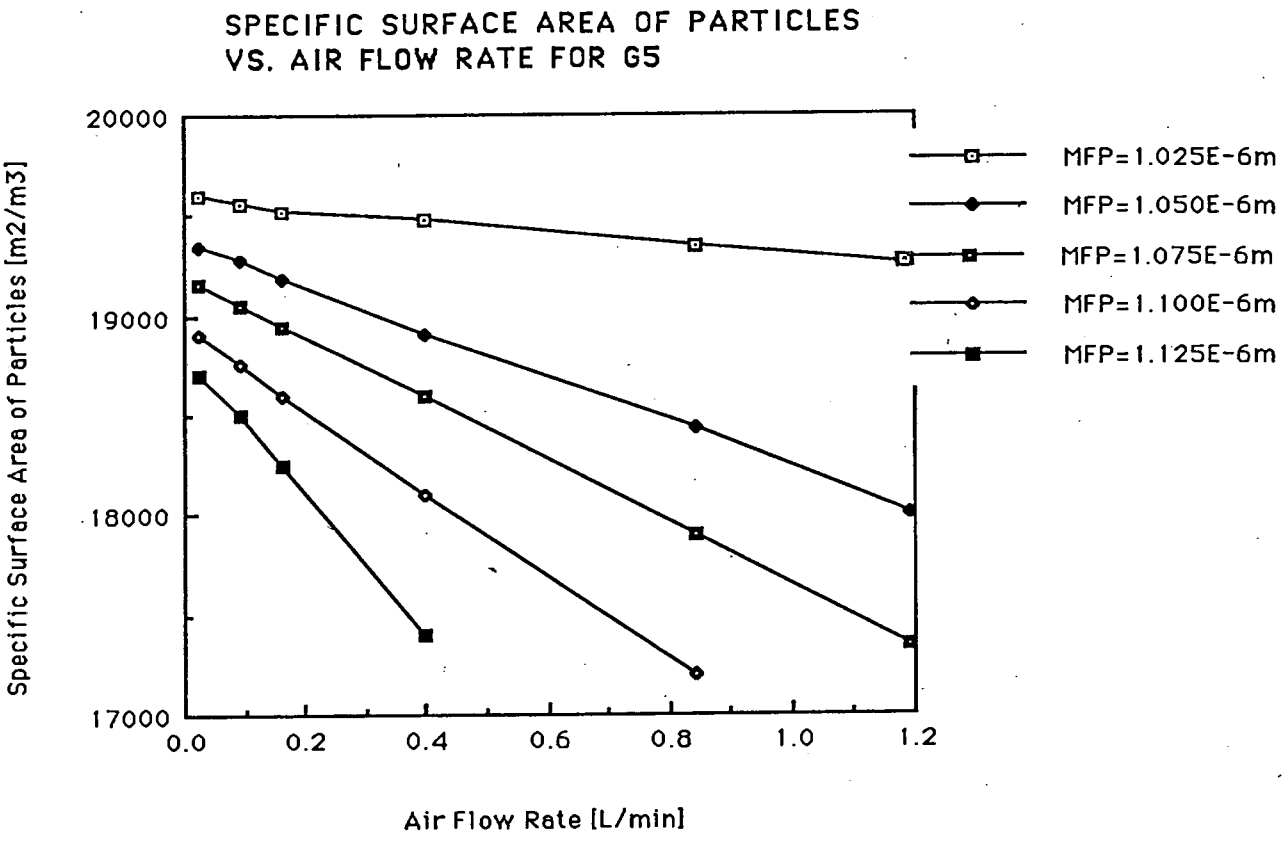

Figure 5.12 Specific Surface Area of Particles vs. Mass Flow Rate for Specimen G

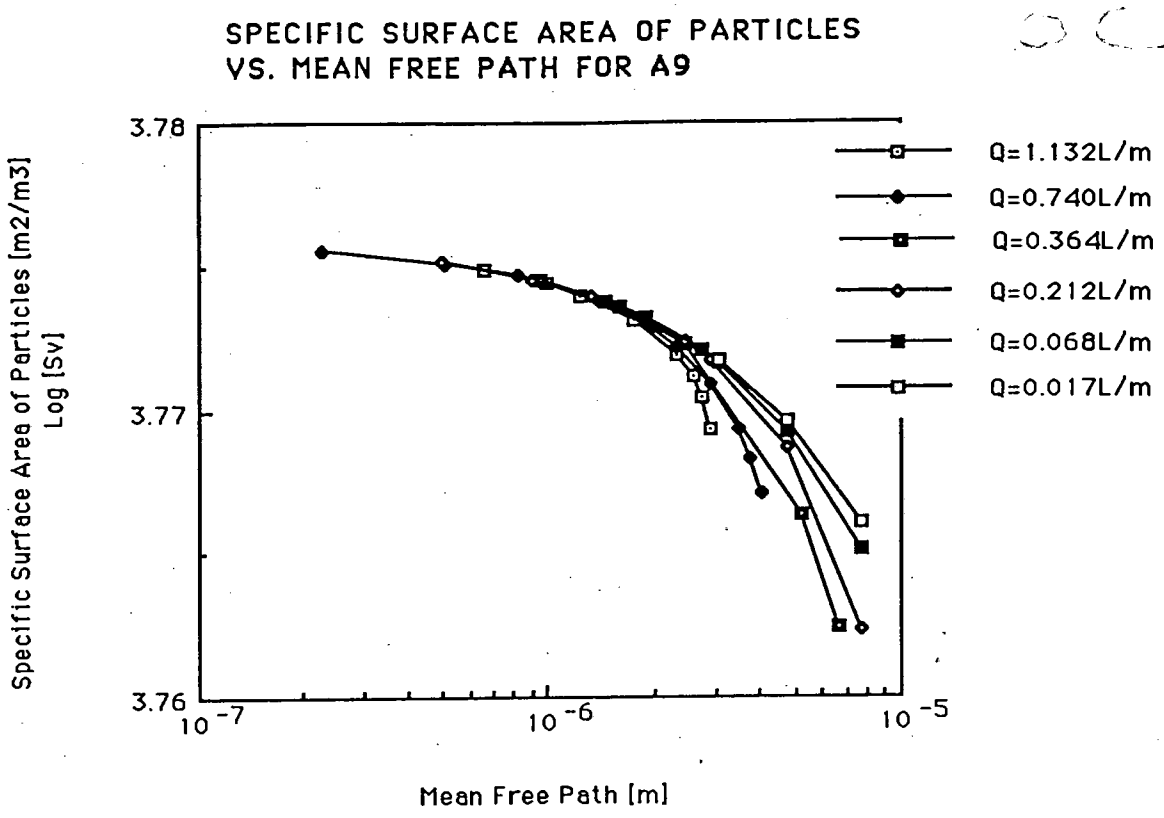

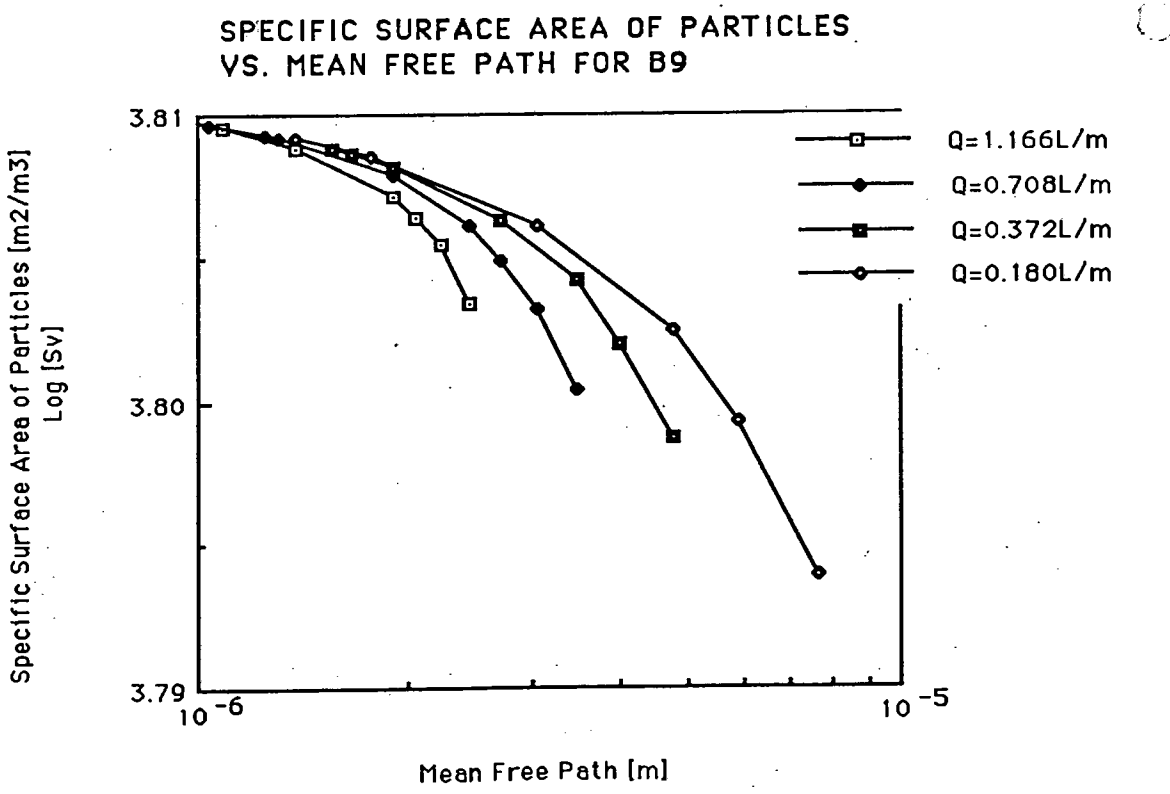

Figure 5.13 Specific Surface Area of Particles vs. Mean Free Path for Specimens A and B

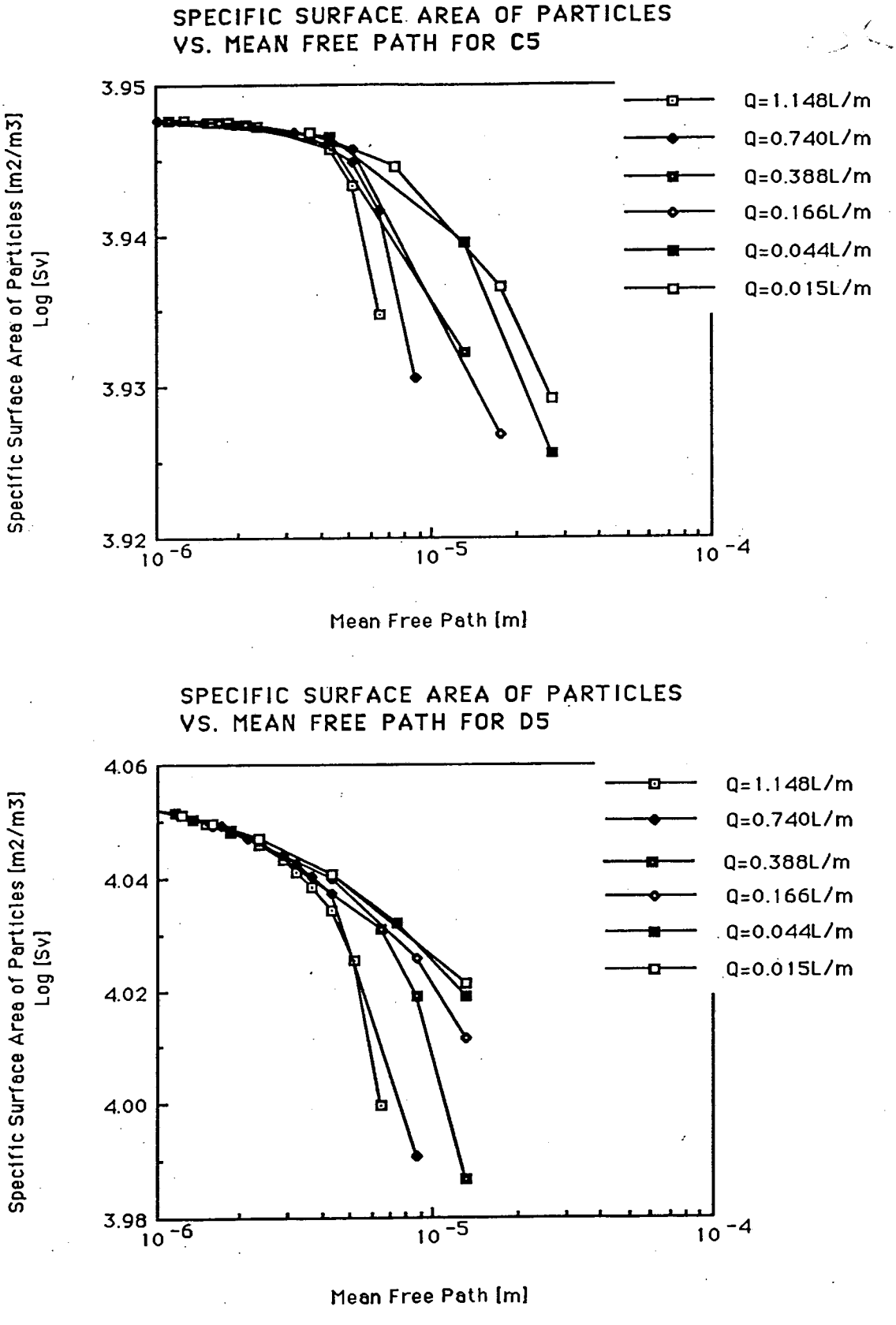

Figure 5.14 Specific Surface Area of Particles vs. Mean Free Path for Specimens C and D

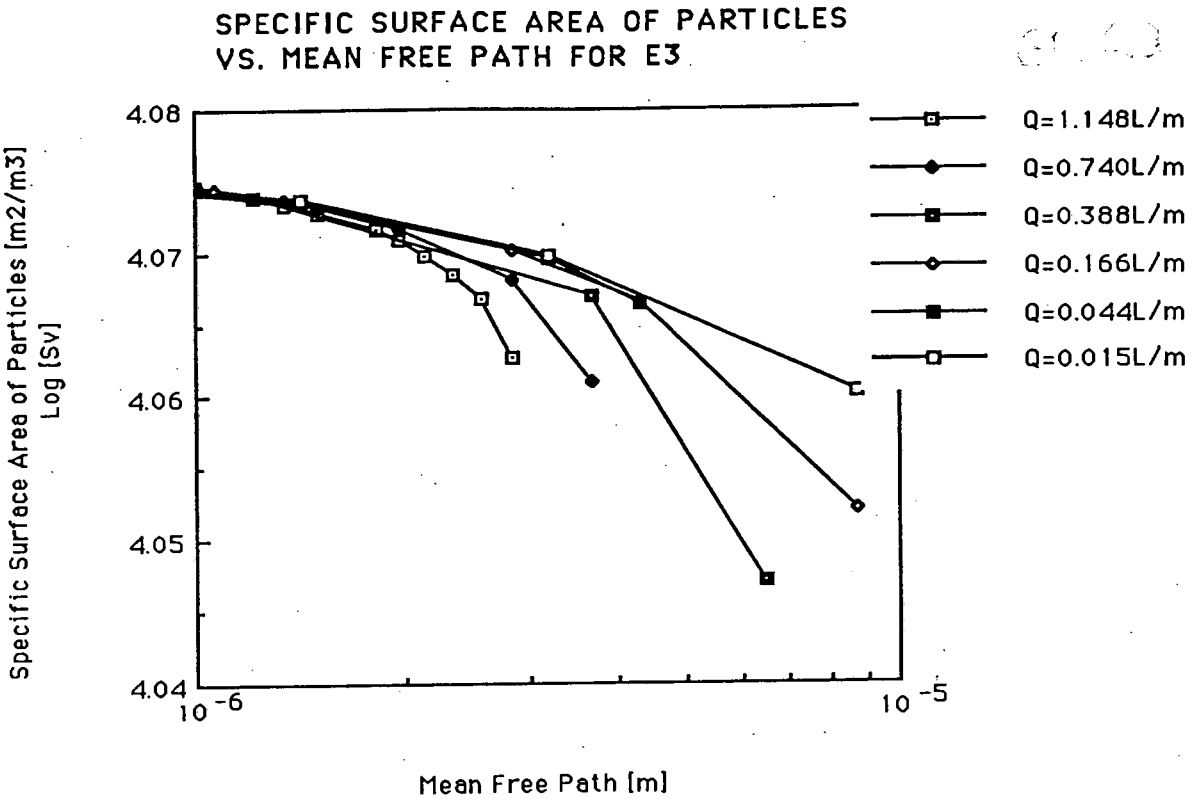

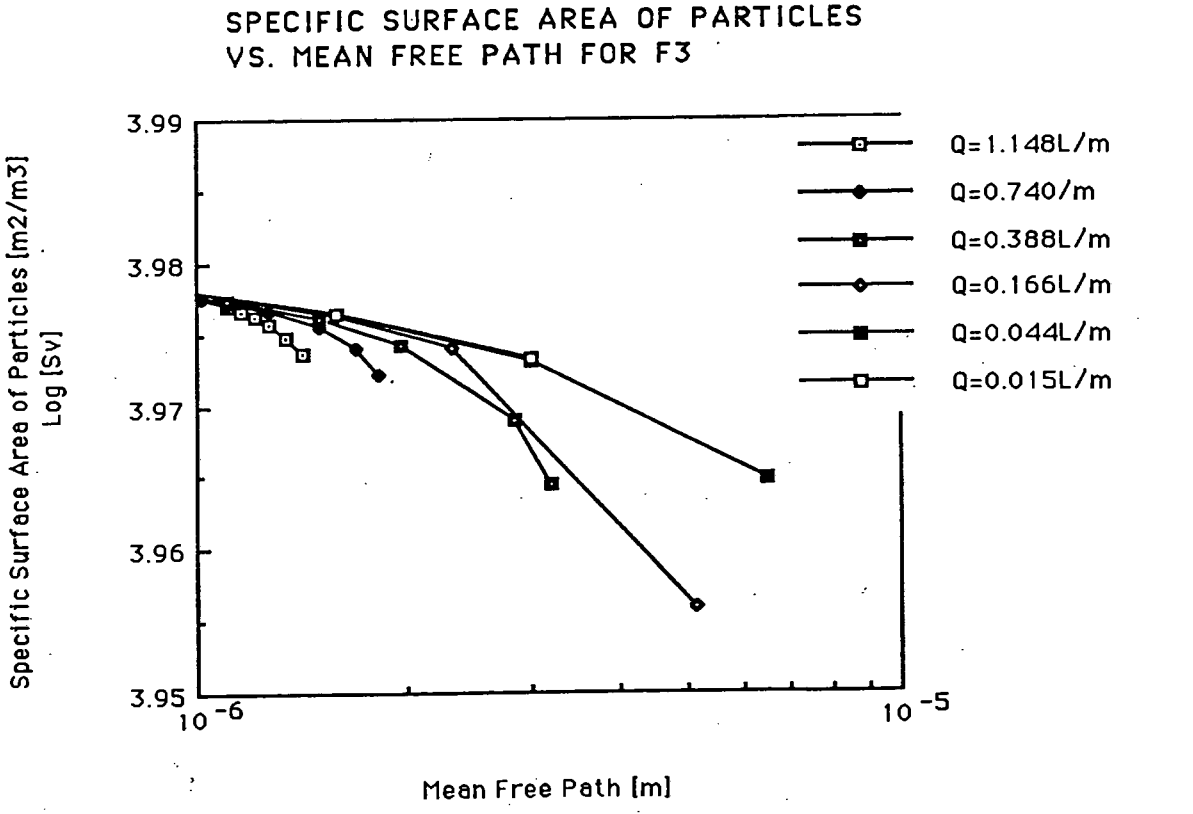

Figure 5.15 Specific Surface Area of Particles vs. Mean Free Path for Specimens E and F

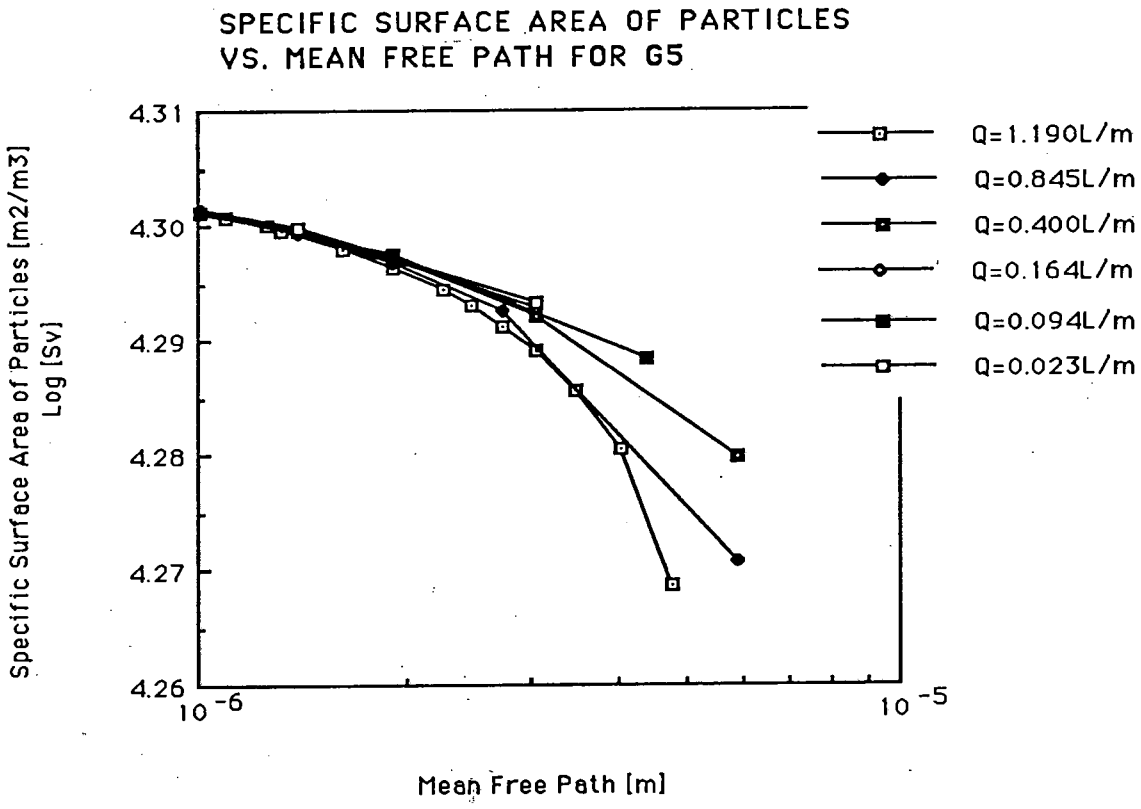

Figure 5.16 Specific Surface Area of Particles vs. Mean Free Path for Specimen G

Table 5.6 Specific Surface Area of Particles vs. Mean Free Path for Specimens A, B, C and D

ecimen A		Specimen B		Specimen C		Specimen D	
MFP, m	Sv, m2/m3	MFP, m	Sv, m2/m3	MFP, m	Sv, m2/m3	MFP, m	Sv, m2/m3
8699E-06	5849.83244	2.4589E-06	6288.44914	6.4718E-06	8606.07083	6.4608E-06	9994.55339
2.715E-06	5866.2079	2.2413E-06	6355.23533	5.1617E-06	8777.44877	5.153E-06	10598.9502
2.576E-06	5878.56635	2.0591E-06	6383.86825	4.2927E-06	8823.02592	4.2855E-06	10820.5512
3367E-06	5894.18711	1.9043E-06	6400.97104	2.3308E-06	8856.02681	3.668E-06	10921.0281
7634E-06	5925.12751	1.384E-06	6435.98184	1.9705E-06	8858.96042	3.206E-06	10994.6174
2413E-06	5941.49955	1.087E-06	6448.23328	1.8292E-06	8859.90771	2.8474E-06	11045.7259
9562E-07	5947.34235	8.9493E-07	6454.81651	1.7067E-06	8860.67425	2.3269E-06	11113.3546
5737E-07	5954.8349	3.4694E-06	5911.64952	1.5997E-06	8861.24359	1.8261E-06	11172.0422
0151E-06	5622.28883	3.0514E-06	6280.04694	1.2788E-06	8862.59	1.5027E-06	11209.9556
7183E-06	5737.33131	2.7233E-06	6352.61762	9.465E-07	8863.40909	1.344E-06	11228.4527
4624E-06	5803.53274	2.4589E-06	6380.36252	9.1263E-07	8863.46279	8.796E-07	11282.3371
8699E-06	5886.25728	1.9043E-06	6419.57922	7.741E-07	8863.61275	7.2856E-07	11300.0701
3367E-06	5910.18607	1.3123E-06	6443.2276	7.5129E-07	8863.62843	8.6584E-06	9790.22696
9706E-06	5923.91727	1.2476E-06	6445.42283	8.6731E-06	8522.03232	4.2855E-06	10893.167
.416E-06	5938.65682	1.0422E-06	6451.68394	6.4718E-06	8743.20005	3.668E-06	10969.5253
1763E-07	5951.62166	4.7786E-06	4672.80829	5.1617E-06	8808.13738	3.206E-06	11027.0656
1059E-07	5957.8529	4.0201E-06	6245.23829	3.6742E-06	8840.35609	2.8474E-06	11068.7086
2.271E-07	5963.43022	3.4694E-06	6338.64281	3.2114E-06	8847.32872	2.132E-06	11144.6015
7043E-06	24851.1394	2.7233E-06	6393.76308	1.5052E-06	8861.77582	1.597E-06	11203.2801
6811E-06	4764.47832	1.9043E-06	6426.90153	1.1115E-06	8863.08998	1.344E-06	11231.4483
5.279E-06	5757.21299	1.6553E-06	6435.00511	1.0224E-06	8863.28645	8.6467E-07	11284.8429
4505E-06	5916.32347	1.5538E-06	6438.08134	8.8109E-07	8863.51164	6.3735E-07	11311.1379
1.457E-06	5939.09812	7.6747E-06	3861.76357	6.7208E-07	8863.66111	3.145E-07	11349.581
5772E-07	5949.16722	5.8899E-06	6232.29192	5.4322E-07	8863.64369	1.3122E-05	9701.75143
7043E-06	5669.33574	4.7786E-06	6319.19043	4.1842E-07	8863.54459	8.6584E-06	10447.8547
7777E-06	5859.79531	3.0514E-06	6395.73489	3.3578E-07	8863.43372	6.4608E-06	10734.9957
8699E-06	5910.3585	1.7711E-06	6433.5819	1.7707E-05	7980.87364	2.3269E-06	11131.8885
4505E-06	5919.31687	1.384E-06	6443.9147	1.3144E-05	8556.33535	1.8261E-06	11182.7004
3405E-06	5941.87719	1.9482E-05	6233.51274	4.2927E-06	8834.97349	1.1602E-06	11252.8567
0597E-07	5950.29877	1.407E-05	6318.36449	3.6742E-06	8843.69068	8.2275E-07	11290.2574
9551E-07	5958.23181	1.1012E-05	6355.45645	2.1356E-06	8858.49402	5.0973E-07	11326.323
7043E-06	5810.76761	9.0452E-06	6402.9344	1.1115E-06	8863.10957	3.9199E-07	11340.3008
7777E-06	5878.1317	7.6747E-06	6434.99296	6.9028E-07	8863.65732	1.3122E-05	10273.7572
0435E-06	5910.62642	5.8899E-06	6444.55264	2.5261E-07	8863.28442	8.6584E-06	10608.7062
2.715E-06	5917.01863	1.9482E-05	6404.25709	1.7707E-05	8448.61068	4.2855E-06	10963.3258
8963E-06	5932.02186	1.407E-05	6435.1947	5.1617E-06	8825.47072	1.7039E-06	11197.082
5956E-06	5937.58527	1.1012E-05	6444.64637	1.7067E-06	8861.04554	8.2275E-07	11290.6215
7043E-06	5834.1088			5.8031E-07	8863.65687	3.145E-07	11349.6633
7777E-06	5883.09188			2.8039E-07	8863.33817	1.3122E-05	10452.3282
0435E-06	5912.20612			2.7126E-05	8424.94459	7.3999E-06	10764.7692
				1.3144E-05	8700.21072	4.2855E-06	10977.988
				4.2927E-06	8839.93982	2.3269E-06	11139.9004
				8.2414E-07	8863.58172	1.2157E-06	11248.6253
				2.967E-07	8863.36752	1.3122E-05	10500.0292
				5.7952E-05	8127.43907	4.2855E-06	10982.6449
				2.7126E-05	8495.34375	2.3269E-06	11141.2422
				1.7707E-05	8641.09812	1.597E-06	11210.0923
				7.4124E-06	8800.80915	1.2157E-06	11248.8368
				3.6742E-06	8846.82146		

Table 5.7 Specific Surface Area of Particles vs. Mean Free Path for Specimens E, F and G

Specimen E		Specimen F		Specimen G	
MFP, m	Sv, m2/m3	MFP, m	Sv, m2/m3	MFP, m	Sv, m2/m3
2.8522E-06	11554.0415	1.4165E-06	9411.7251	4.7912E-06	11047.8474
2.5653E-06	11662.4441	1.3417E-06	9436.87513	4.0355E-06	18421.7171
2.3308E-06	11709.6981	1.2745E-06	9456.28401	3.4857E-06	19076.7917
2.1356E-06	11744.5027	1.2136E-06	9467.0231	3.0677E-06	19348.1137
1.9705E-06	11772.2602	1.1583E-06	9474.92224	2.7393E-06	19489.1998
1.8292E-06	11794.051	1.1078E-06	9482.66549	2.4744E-06	19591.2075
1.5052E-06	11825.6408	9.7967E-07	9494.26681	2.2562E-06	19663.6745
1.3463E-06	11840.5186	8.2135E-07	9507.75699	1.9179E-06	19769.117
9.1263E-07	11873.9859	7.2732E-07	9515.00571	1.6152E-06	19852.7476
6.3843E-07	11893.8685	1.823E-06	9378.54624	1.3229E-06	19928.9288
3.6742E-06	11508.951	1.701E-06	9419.80712	1.2579E-06	19945.8659
2.8522E-06	11697.8351	1.5002E-06	9452.42214	1.0962E-06	19986.5366
1.9705E-06	11790.8274	1.2745E-06	9474.11506	1.0097E-06	20008.6219
1.5052E-06	11832.491	1.1078E-06	9489.05949	9.0278E-07	20034.6788
1.0224E-06	11867.7762	1.019E-06	9496.09371	7.6601E-06	379561.306
7.2979E-07	11888.1363	8.2135E-07	9509.94092	5.8951E-06	17940.543
3.867E-07	11911.3568	6.3627E-07	9522.27428	2.7393E-06	19580.3102
3.5944E-07	11913.2076	5.4139E-07	9528.2768	1.9179E-06	19794.9459
2.5261E-07	11920.3968	4.6255E-07	9533.23075	1.395E-06	19921.6273
2.3623E-07	11921.5068	4.1701E-07	9536.04346	1.0097E-06	20011.397
6.4718E-06	11144.8833	2.8573E-07	9543.9964	6.6732E-07	20092.9092
3.6742E-06	11669.4827	2.1188E-07	9548.45373	4.7966E-07	20137.9435
1.2177E-06	11855.6303	1.8031E-07	9550.35166	4.2401E-07	20151.4969
8.8109E-07	11878.5087	3.2006E-06	9216.82542	1.0934E-05	-627.08349
6.7208E-07	11892.4388	2.8426E-06	9310.91503	5.8951E-06	18871.1366
5.1059E-07	11903.2023	1.9639E-06	9421.74518	3.0677E-06	19582.5465
2.5261E-07	11920.4232	1.5002E-06	9463.90285	1.9179E-06	19820.8817
8.6731E-06	11272.9388	1.1078E-06	9492.61221	1.395E-06	19931.718
4.2927E-06	11657.0686	5.5317E-07	9527.98794	7.6739E-07	20071.1863
2.8522E-06	11752.2249	4.1701E-07	9536.18669	6.6732E-07	20094.2416
1.3463E-06	11849.1309	3.7405E-07	9538.79209	4.7966E-07	20138.5696
1.0651E-06	11867.2741	3.1397E-07	9542.39235	4.2401E-07	20151.9267
5.9382E-07	11897.8412	2.1013E-07	9548.58583	7.6601E-06	18817.7983
4.1842E-07	11909.4086	5.1443E-06	9036.55046	3.0677E-06	19619.9806
4.2927E-06	8429.05013	2.3229E-06	9419.15461	1.395E-06	19936.6111
3.2114E-06	11738.7491	1.5943E-06	9466.4072	9.7133E-07	20026.725
1.4213E-06	11845.6898	9.7967E-07	9503.35387	8.7201E-07	20048.6224
3.1503E-07	11916.2973	6.2073E-07	9524.42853	6.6732E-07	20094.9185
2.7126E-05	10869.9897	4.1701E-07	9536.38448	4.7966E-07	20138.7902
8.6731E-06	11491.3014	2.957E-07	9543.53784	4.0393E-07	20156.9114
3.2114E-06	11744.9398	5.7756E-05	10020.9338	1.3905E-05	18109.2015
1.4213E-06	11846.3625	2.7035E-05	7304.4019	4.381E-06	19422.9329
3.1503E-07	11916.3095	6.4499E-06	9222.56998	1.9179E-06	19835.3306
		3.011E-06	9397.55904	7.6739E-07	20072.3586
		1.5943E-06	9471.27076	6.6732E-07	20095.1055
		9.7967E-07	9504.6214	3.0699E-07	20180.51
		6.2073E-07	9524.82441	1.3905E-05	18434.148
		4.5428E-07	9534.36848	3.0677E-06	19639.9092
		2.7035E-05	8597.66294	1.395E-06	19939.3907
		3.011E-06	9401.92659	4.3855E-07	20148.7196
		1.5943E-06	9471.93929	3.0699E-07	20180.5395
		9.7967E-07	9504.814	2.4758E-07	20195.192
		6.2073E-07	9524.85451		
		4.5428E-07	9534.38322		

case without this mean free path effect. This means that the fractal nature of the pore structure was revealed at long mean free paths and extremely low flow rates, as seen from the log-log plots of the specific surface area versus the mean free path. The mean free path of gas molecules increased and thus the effective surface area S_V and porosity of the specimen decreased as total pressure decreased. These contributed to the increase in pressure drop at very low pressures.

According to fractal geometry, if certain phenomenon has a fractal nature, the following equation must be satisfied:

$$N(r) \quad \alpha \quad r^{-D} \qquad (5.1)$$

In the above equation, the index D expresses the complexity of the phenomenon, and is called the fractal dimension.

This concept can be applicable if equation (5.1) holds between S_V and λ in large λ region. In figures 5.5-5.8, the S_V curve was not straight over the whole λ region, but in the slip-flow region it was essentially straight within experimental accuracy, thus showing that the specific surface area S_V and the pore structure had a fractal nature. The slope for each specimen was determined and listed in table 5.9 together with the fractal dimensions obtained separately from two-dimensional images of the corresponding specimen.

As seen from the table, the results obtained from this new three- dimensional approach via pressure drop measurement revealed a quantitative picture of the pore structure. The fractal dimensions of specimens with larger diameter pores showed a bigger discrepancy between the values from image counting technique and by the S_V slope than the smaller ones do. This implies that specimens with bigger pores have more kinked corners and numerous smaller local cavities than those with smaller pores. This is probably due to the bigger grain sizes of specimens with bigger pore sizes. The fractal dimensions obtained by two-dimensional approach can not illustrate the real pore structure in depth, and the results obtained from the three-dimensional approach should indicate the real phenomenon better.

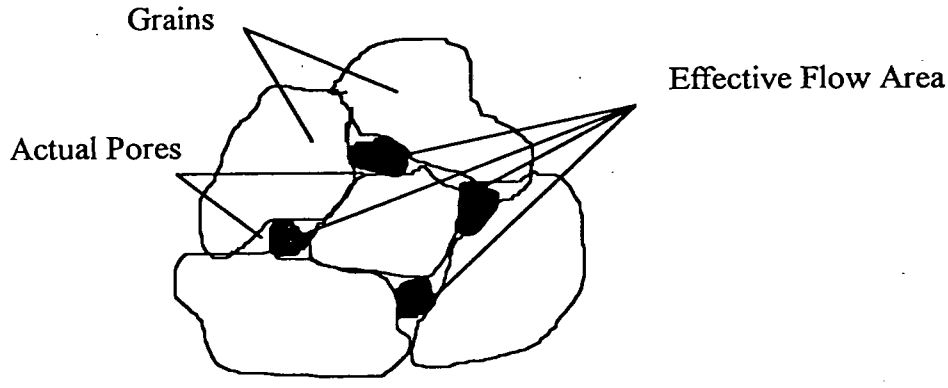

Figure 5.17 Effective Flow Area

Table 5.8 Calculated Value of Knudsen Number for Each Specimen

Specimen	A	B	C	D	E	F	G
Knudsen Number	0.003-0.115	0.019-0.142	0.006-0.706	0.005-0.298	0.009-0.692	0.016-0.699	0.014-0.82

Table 5.9 Relationship of Physical Properties and Fractal Dimensions Obtained from Counting and Measurement

Specimen / Parameters	A	B	C	D	E	F	G
Permeability, K *10^{-6} [m^2/s Pa]	4.20	1.60	1.25	1.00	0.6	0.5	0.4
Mean Pore Diameter [d_e]	135	108	76.8	69.7	51.2	39.2	34
Porosity, ε [-]	24.1	21.7	26.6	20.9	16.4	15	21.4
Fractal Dimension, D [Counting]	1.75	1.73	1.71	1.70	1.67	1.64	1.56
Fractal Dimension, D [S_V slope]	1.30	1.20	1.25	1.23	1.46	1.43	1.43
Difference Between The Two Fractal Dimensions %	25.71	30.63	26.9	27.6	12.57	12.8	8.33

3. Relationship of Physical Properties and Fractal Dimension.

As seen from the table, the fractal dimension obtained from the proposed three-dimensional analysis ranges from 1.20 to 1.46. The fractal dimensions are larger for specimens with larger pores and smaller with smaller pores. However, the fractal dimensions obtained from two-dimensional images are larger than 1.5 for every specimen. So, the interpretation of the fractal dimension obtained via pressure drop measurement across the porous medium shows better accuracy and reveals a quantitative picture to visualize the three-dimensional information of the internal pore structure.

Permeability, K is the physical property of the specimen that governs the through flow rate of air Q, at a certain pressure drop (ΔP). In table 5.9 and figure 5.18, the permeability value obtained experimentally for each specimen at the same absolute total pressure in the long mean free path region was plotted against the fractal dimension obtained from the counting technique. The permeability was found to increase as the fractal dimension increased which meant that permeability was closely related to fractal dimension of the pore structure.

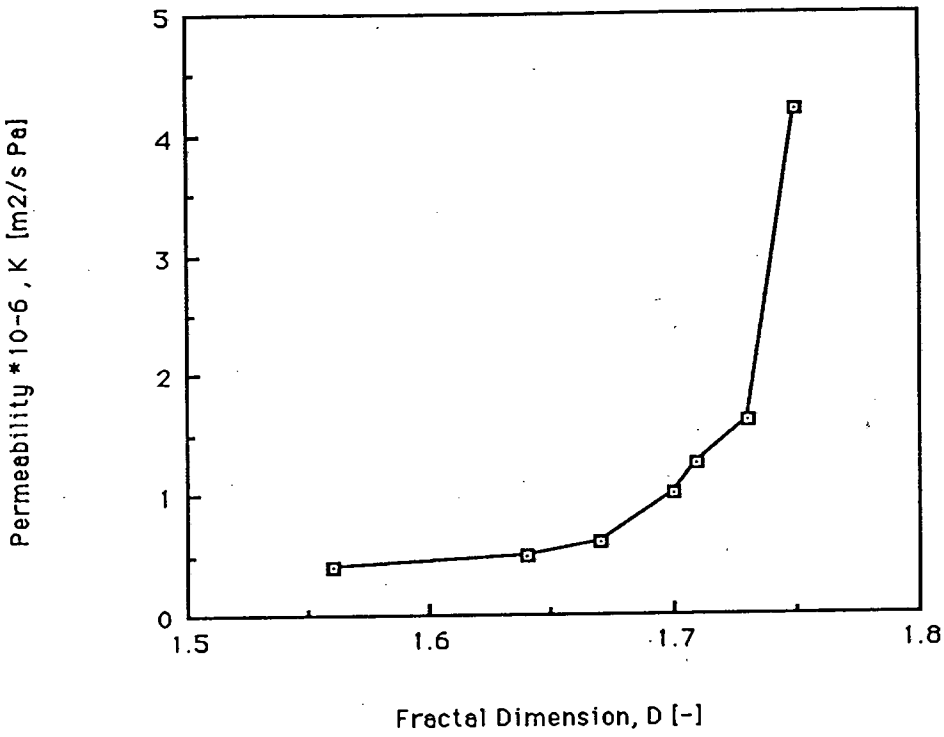

Figure 5.18 Permeability vs. Fractal Dimension

4. Comparison of Two- and Three-Dimensional Fractal Dimensions.

The relationship between the counted number of grids that wholly or partially contained the pores, N(r) and the similarity ratio r, was plotted on log-log scales as shown in figure 4.5. The two-dimensional (visual) fractal dimension was calculated from the slope of the corresponding straight line in the figure, and the pore shape was shown to have a fractal nature. Table 5.9 and figure 5.18 showed the relations between the calculated permeability and the two fractal dimensions obtained visually and experimentally for all specimens. Obviously, permeability increased as either fractal dimension increased. Table 5.9 compared the fractal dimensions obtained

visually from counting and from the experimentally S_V slope. The discrepancy indicated the existence of stagnant air pockets and dead-end void. As seen from the table , the discrepancy was larger for specimens that have larger fractal dimensions.

5. Comparison of Two-Dimensional Pore Area by Image Analysis and Three-Dimensional Pore Area by Pressure Drop.

Image analysis is an important technique to measure directly the pore shape geometry using an image analyzer, but it can only measure in two-dimensional view. The main components of the system are a video camera, analog to digital signal conversion circuitry to convert the video signal to digital one, computer system with dedicated image data memory separate from the system program memory, display monitors for program control and image display, and peripheral devices to provide hard copy of the processed data and image printout. Individual and total pore areas, frame area (total pore area and total granule area), perimeter length, maximum and minimum values and standard deviation were the output obtained from figures 4.2-4.4 using the image analyzer. The ratio of total pore area to frame area of each specimen was summarized in table 5.10.

The experimental pore area was obtained from the value of the specific surface area and can be expressed as average pore radius in the long mean free path region of each specimen. Therefore, the experimental pore area was calculated by the following equation:

$$S_{experiment} = \lambda^2 N(r) \qquad (5.2)$$

Table 5.9 summarized the two pore areas obtained around the lowest air flow rate region of each specimen.

Table 5.10 also showed the relative difference in percentage between these two areas which indicated the existence of stagnant air pockets and dead-ends as stated in connection with table 5.9. The differences in both tables were nearly the same. Due to the presence of highly regular pore channels, rarefied air flow through the channels were not fully distributed over the whole cross-sectional area, caused by inaccessible stagnant air pockets at some kinks corners of the pores. From these two tables, it was concluded that the three-dimensional

approach gave a physically more meaningful picture of pore structure, especially when the fractal dimension was large. This suggested that the mysterious of air pocket could be discovered by applying the concept of fractal dimension to the measurement of air flow through porous specimens and to image analysis of the cut specimens.

Table 5.10 Comparison of Image Pore Area and Experimental Pore Area

Parameter \ Specimen	A	B	C	D	E	F	G
Image Pore Area, ε[-] (S_{Image})	0.361	0.311	0.316	0.319	0.289	0.262	0.279
Experimental Pore, ε[-] Area ($S_{experiment}$)	0.270	0.217	0.232	0.231	0.254	0.230	0.256
Difference Between These Two Pore Areas, %	25.21	30.22	26.58	27.58	12.11	12.22	8.24

Effect of Matrix Content on the Physical Properties and Pore Structure of Porous Spinel Refractories.

1. Micro-Structure Observation of Sintered Body.

Figure 5.19 showed some of the microphotographs of various specimens taken by means of reflecting microscopy. Evidently boundary cracks tended to proliferate and pore sizes tended to shrink as the matrix contents increased. For the system TA 5, containing 5% TiO_2 and Al_2O_3 (molar ratio 1.0) by total weight as matrix and 95% of $Mg{\cdot}O{\cdot}Al_2O_3$ as aggregates, pore sizes were relatively large and co-sintering between the aggregates and the matrix additive was not clearly recognizable. Compared to the other TA systems, only a few glossy areas were detected locally on the aggregates. For system TA 15, boundary cracks (BC) on the aggregates and along the contact areas of the aggregates particles as well as internal cracks (C) were clearly visible. Typical pore sizes were smaller than those of TA15 while most pores were apparently isolated though linked through cracks, thus

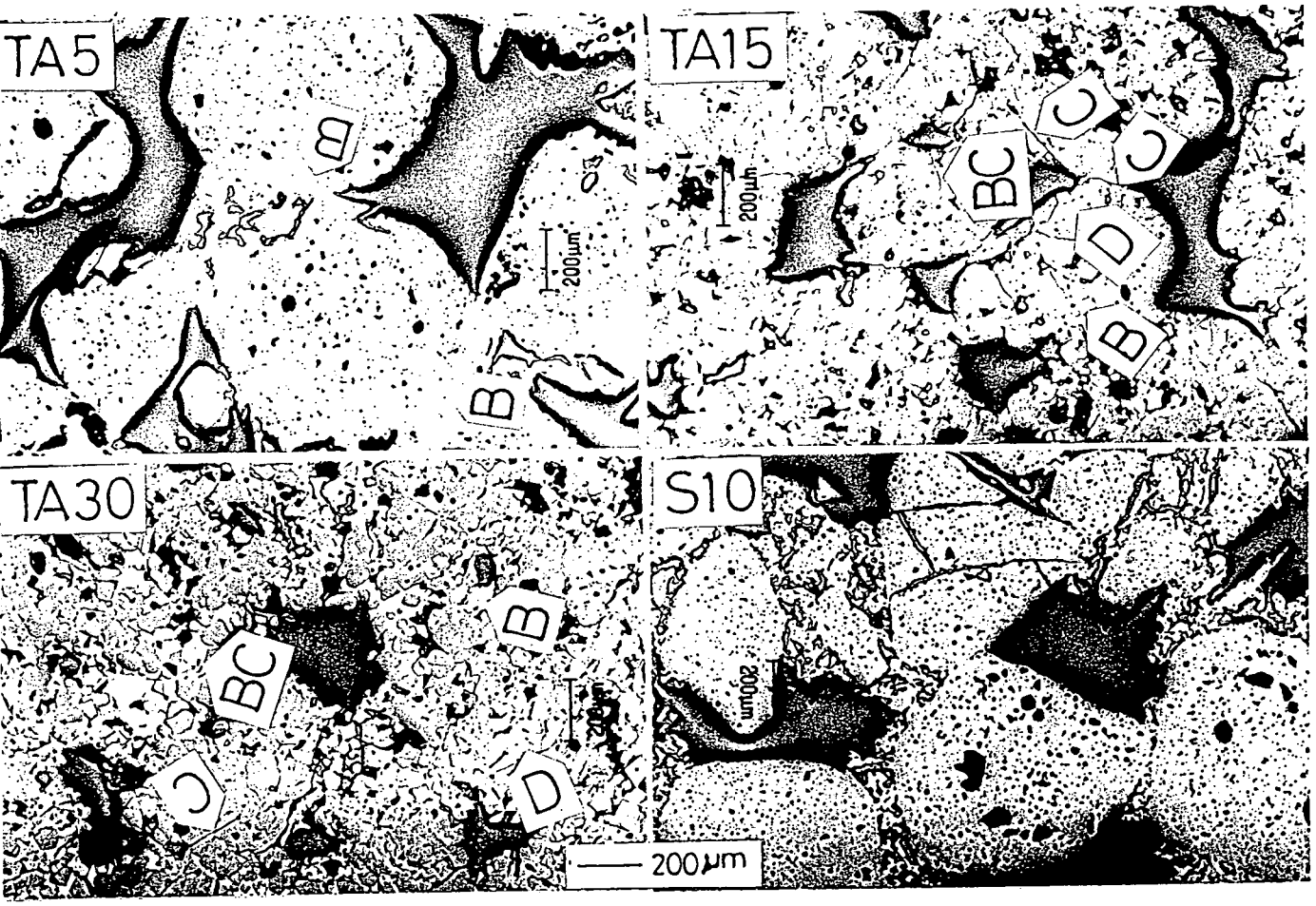

Figure 5.19 Photomicrographs of Some Typical Specimens (B: Bright glossy area, D: Dark glossy area, BC: Boundary crack, C: Crack)

producing more interconnected pores. The glossy areas were observed at the boundary of the aggregate particles. In system TA 30, the fused areas between the aggregate particles increased to the extent that one could not readily recognize where the individual aggregate particles were located. The pore sizes became even smaller, but boundary cracks as well as glossy areas substantially increased as compared to TA 15.

On the other hand, for the system containing 10 wt. % $MgO{\cdot}Al_2O_3$ powder as matrix and 90 wt.% MgO. Al_2O_3 as aggregate, hereafter called S10, the matrix additive existed along the contact areas between aggregate particles and on the individual aggregate particles, thus its presence was clearly visible, without changes in their original pore shapes.

2. EPMA and X-ray Diffraction.

Figure 5.20 showed an EPMA analysis of the spatial distribution of metals among the aggregate and the matrix in some local regions of the specimens. For the TA5 system, Ti distributed mainly along the boundary of the aggregate particles. For system TA15, Ti similarly distributed in the glossy areas where Al and Mg were clearly observed. For TA30 the spatial distribution was again similar though Ti distributed more evenly .

Table 5.11 summarized the X-ray diffraction results for the specimens. $Al_2O_3{\cdot}TiO_2$ was detected in all specimens except TA30 and the value of its X-ray intensity rose as the matrix content increased but its presence was not detected for the system TA30. Meanwhile, $MgO.Al_2O_3$ - 2 $Mg{\cdot}TiO_2$ solid solution diminished, whereas $Al_2O_3{\cdot}TiO_2$ - $MgO{\cdot}2\ TiO_2$ solid solution rose markedly, as the matrix content increased.

The above mentioned results and the microphotos in figure 5.19 combined to indicate that in the glossy areas cohabited $Al_2O_3{\cdot}TiO_2$ - $MgO{\cdot}2TiO_2$ (or $Mg_{0.3}\ Al_{1.4}\ Ti_{1.3}\ O_5$ or $MgAl_8Ti_6\ O_{25}$), Al_2O_3-TiO_2 and $MgO{\cdot}Al_2O_3$-$2MgO{\cdot}TiO_2$ solid solution.

The main reason why $Al_2O_3{\cdot}TiO_2$ was not detected in the TA30 system was that all the $Al_2O_3{\cdot}TiO_2$ produced proceeded to react to form $Al_2O_3{\cdot}TiO_2$ - $MgO{\cdot}2\ TiO_2$.

Table 5.11 Results of the X-ray Diffraction Analysis

Specimen		TA5	TA10	TA15	TA20	TA30	S10
Spinel ($MgO.Al_2O_3$)	*1	5+	5+	5+	5+	5+	5+
Periclase (MgO)		-	-	-	-	-	1^-
Aluminium titanate ($Al_2O_3.TiO_2$)		113	113	138	150	-	-
Solid solution ($MgO.Al_2O_3$-$2MgO.TiO_2$)	*2	125	113	100	100	88	-
Solid solution ($Al_2O_3.TiO_2$-$MgO.2TiO_2$) or $Mg_{0.3}Al_{1.4}Ti_{1.3}O_5$ or $MgAl_8Ti_6O_{25}$		125	325	425	675	813	-

*1 Show the peak intensity of the X-ray, $5^+>5>4>3>2>1>1^-$

*2 Show the count per second of the X-ray intensity

3. Bulk Density and Apparent Porosity.

Figure 5.21 showed the obtained correlation between bulk density, apparent porosity and matrix content. Bulk density gradually diminished as the matrix content increased and then dropped sharply at 20 wt. % content upward. As a result, apparent porosity rose with increase of the matrix content.

The reason why bulk density decreased was that more cracks, both internal and boundary, were observed as the matrix content increased (figure 5.19). Thus the apparent porosity also increased.

4. Compressive Strength of Specimens.

Figure 5.22 showed the relation between the compressive strength and the matrix content. The compressive strength exhibited a maximum value at 10 wt. % matrix content, above which it dropped sharply and approached a constant value over 20 wt. % content. This was due to the proliferation of boundary cracks as the matrix content further increased, as seen from the microphotos in figure 5.19. The maximum compressive strength at 10 wt. % was attributed to the high degree of co-sintering between the particles despite the appearance of fine cracks.

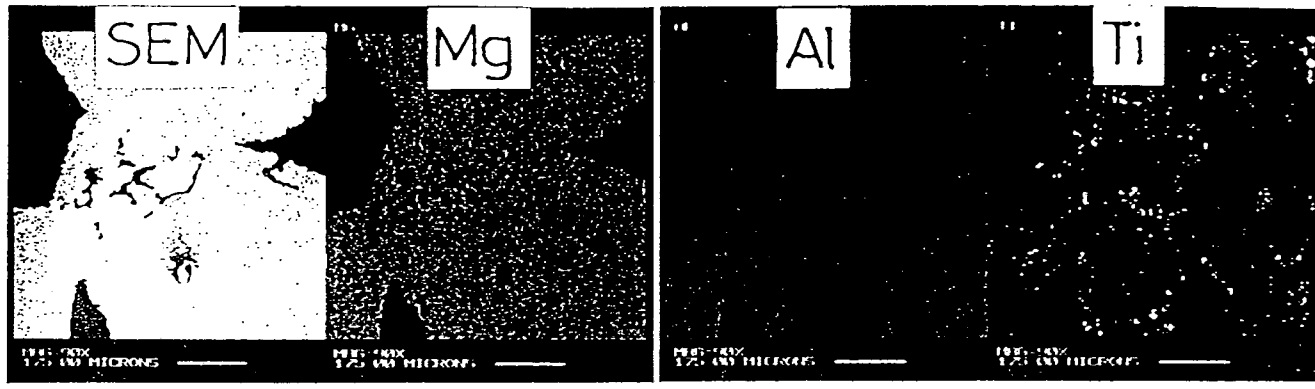

(TA5)

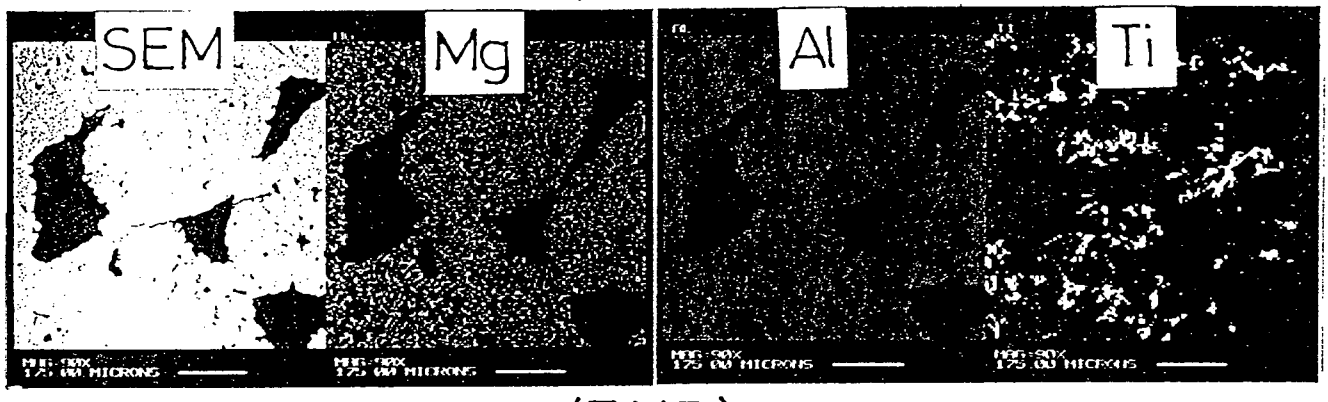

(TA15)

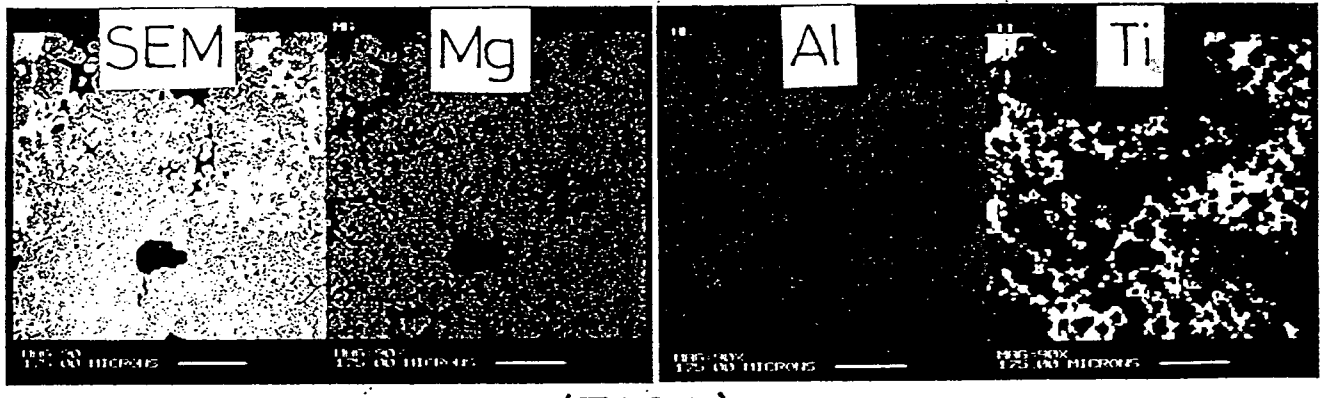

(TA30)

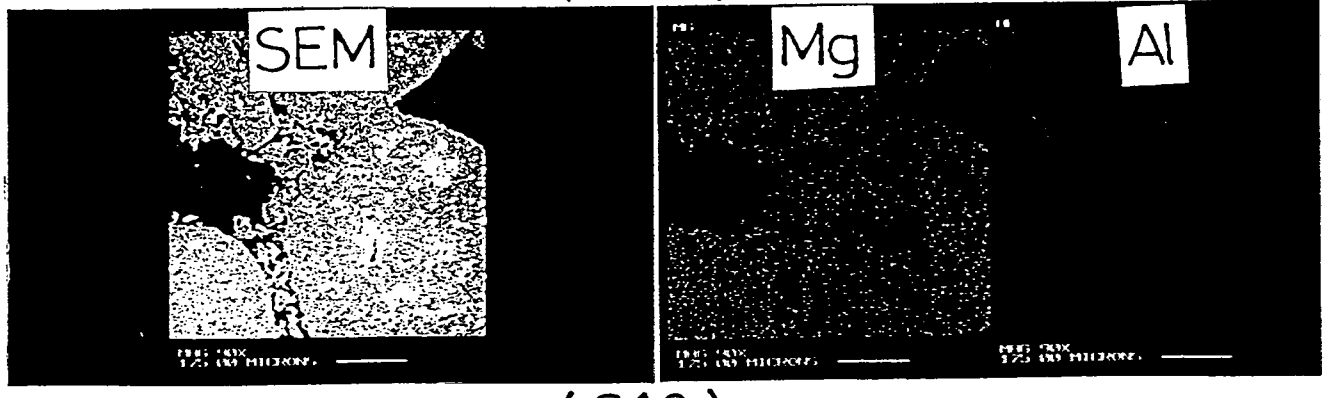

(S10)

Figure 5.20 EPMA Analysis of Specimens

5. Pore Size Distribution and Permeability.

Figure 5.23 showed the relation between mean pore size, permeability and matrix content. Obviously both the mean pore size and permeability exhibited a maximum at about 10 wt. % matrix content, above which both diminished as the matrix content further increased. From figure 5.19 and table 5.11, boundary cracks proliferated and solid solution products became very high, thus causing the aggregate particles to become enlarged and apparently the aggregate phase collapsed, resulting in a reduced mean pore size. In addition, some of the solid solution products could partially or completely block some of the pores, thus further reducing the permeability. A typical correlation among permeability K, apparent porosity P_O, and mean pore size d, was the following Kozeny-Carman equation (Iso, H., et.al. 1985).

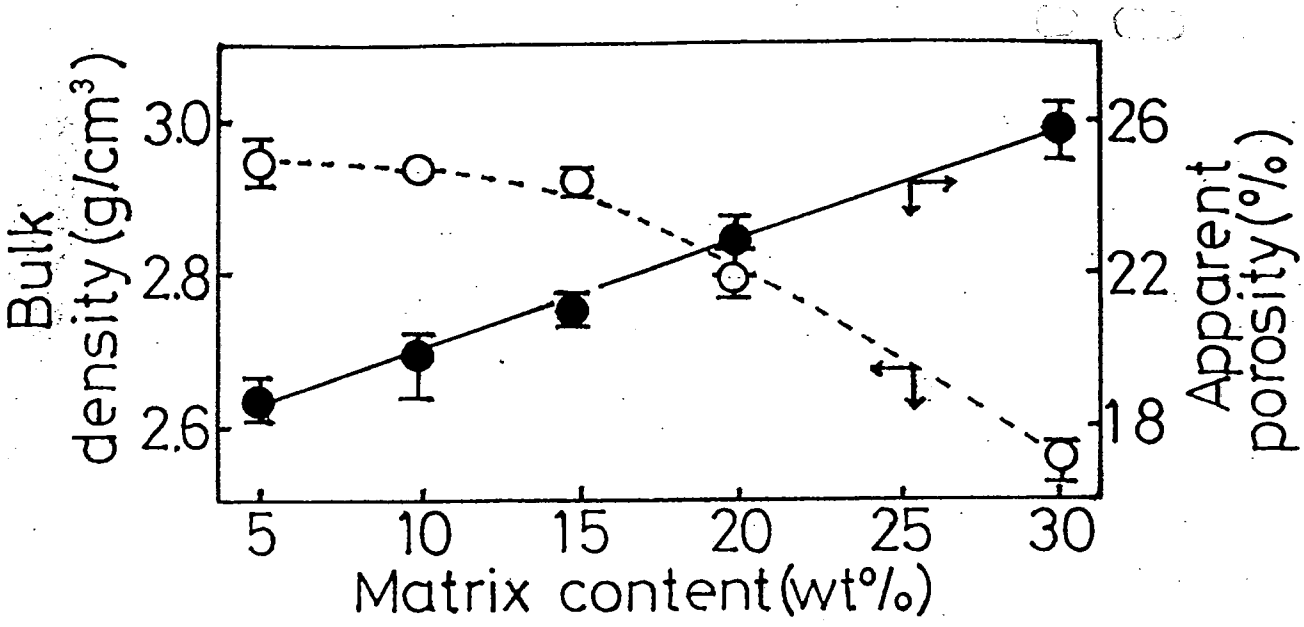

Figure 5.21 Change of Bulk Density and Apparent Porosity against Matrix Content

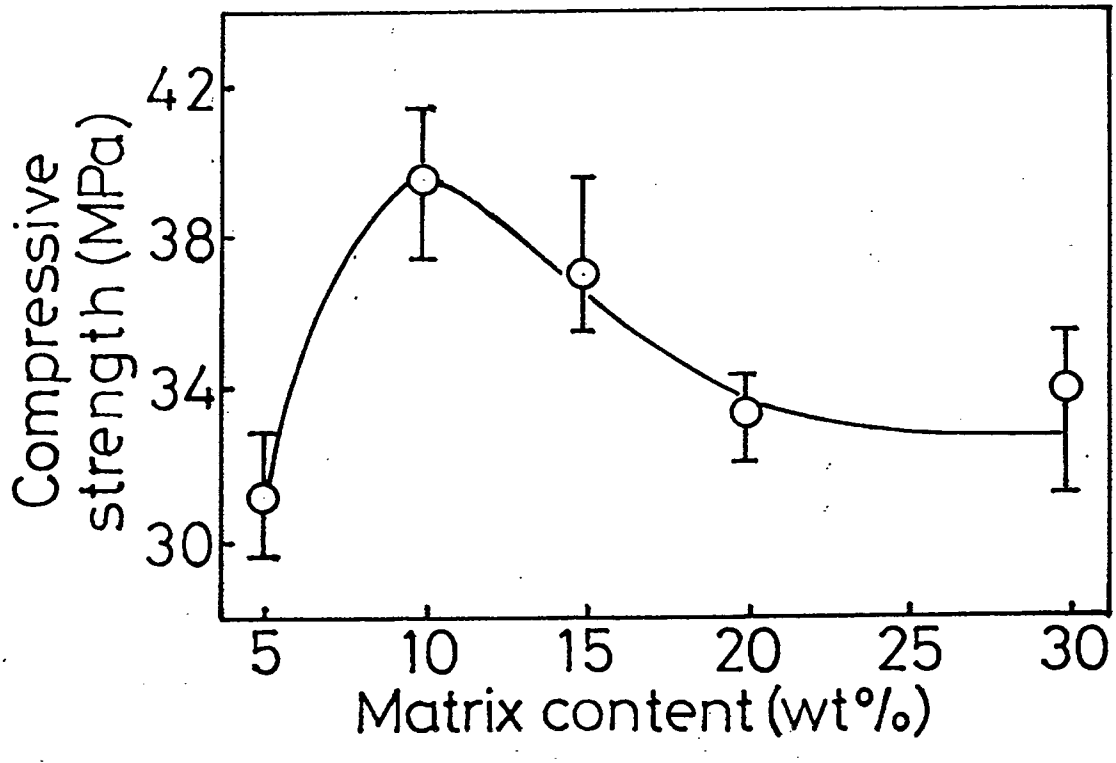

Figure 5.22 Relation between Compressive Strength and Matrix Content

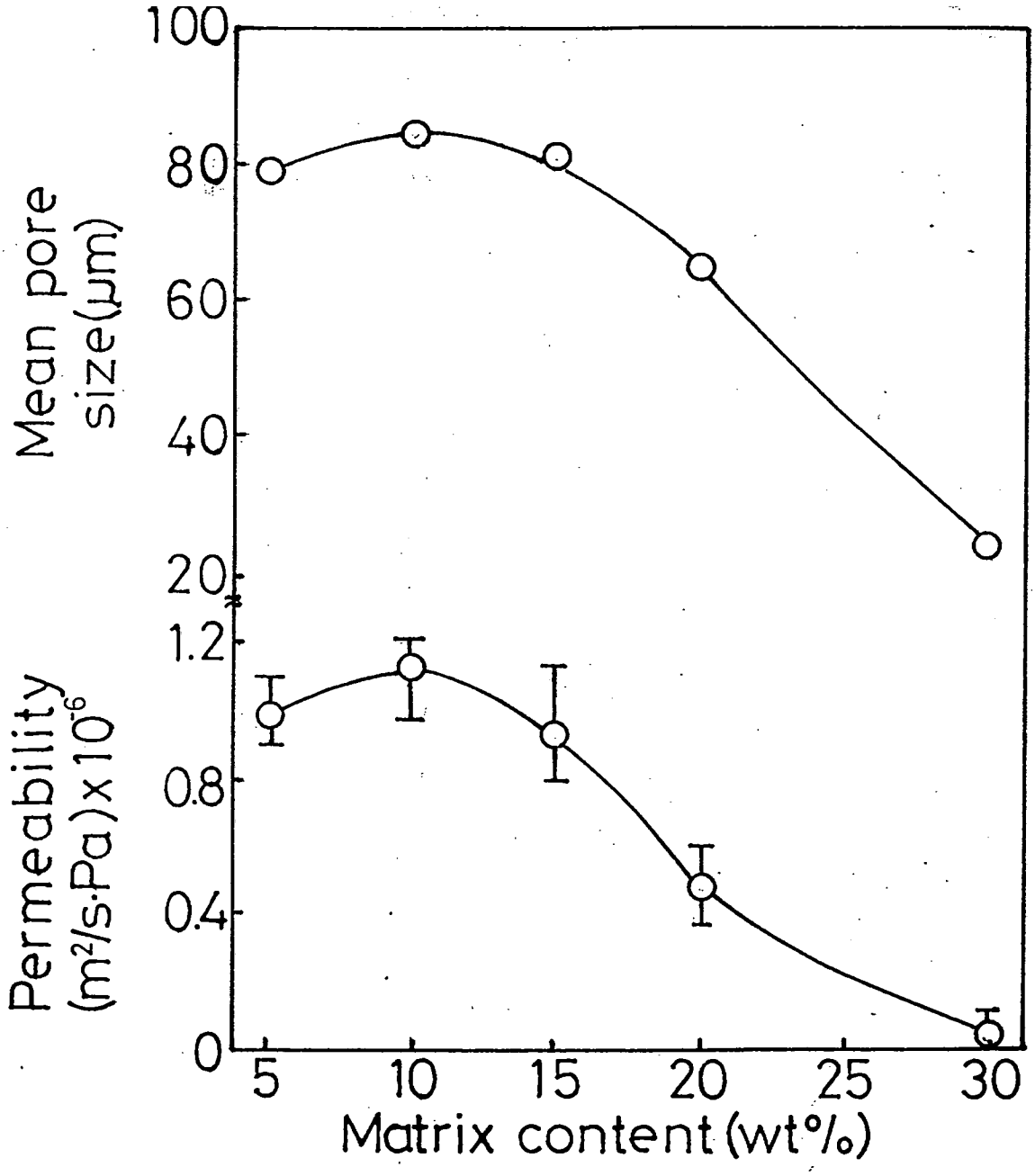

Figure 5.23 Influence of Matrix Content on Mean Pore Size and Permeability

$$K = K_o P_o (\bar{d})^2 \quad (5.3)$$

$$K_o = 1/80\ \mu \quad (\mu \text{ is viscosity of gas}) \quad (5.4)$$

Figure 5.24 showed a log-log plot between K and $\bar{P}_o(d)^2$ in comparison with the Kozeny-Carman plot.

6. Fractal Analysis of Pore Shape.

A fractal is defined as an extremely irregular line or surface formed of an infinite number of similar irregular sections. A fractal has fractional dimension between one and two, or between two and three, dimensions. The extremely irregular pore shape, as represented by the periphery of the pore cross section, may be treated as a fractal.

Let N(r) be the counted number of subsections (squares of side r) containing at least one portion of the pore, when the representative length of each sub-section is r, the so-called similarity ratio.

For a fractal, the following equation holds:

$$N(r) = (\text{Similarity ratio})^{-D} \quad (5.5)$$

Here the fractal dimension, D is defined by:

$$D = -\frac{\log N(r)}{\log (r)} \quad (5.6)$$

The specimens were microphotographed using a reflecting microscope and an example of the fractal counting N(r) was shown in figure 3.8 (chapter 3). In short, the similarity ratios r was halved consecutively from 1/2, 1/4, 1/8 to 1/128 and the number of N(r) was counted as a function of r. The relationship between N(r) and r was plotted on log-log scales as shown in figure 5.25. The fractal dimension was calculated from the slope of the corresponding straight line in figure 5.25. The pore shape for the system TA was found to have a fractal nature (Takayasu, H. 1989). Figure 5.26 showed the relation between the calculated fractal dimension and the matrix content. The fractal dimension of 5 wt. % matrix content was 1.61 and the fractal

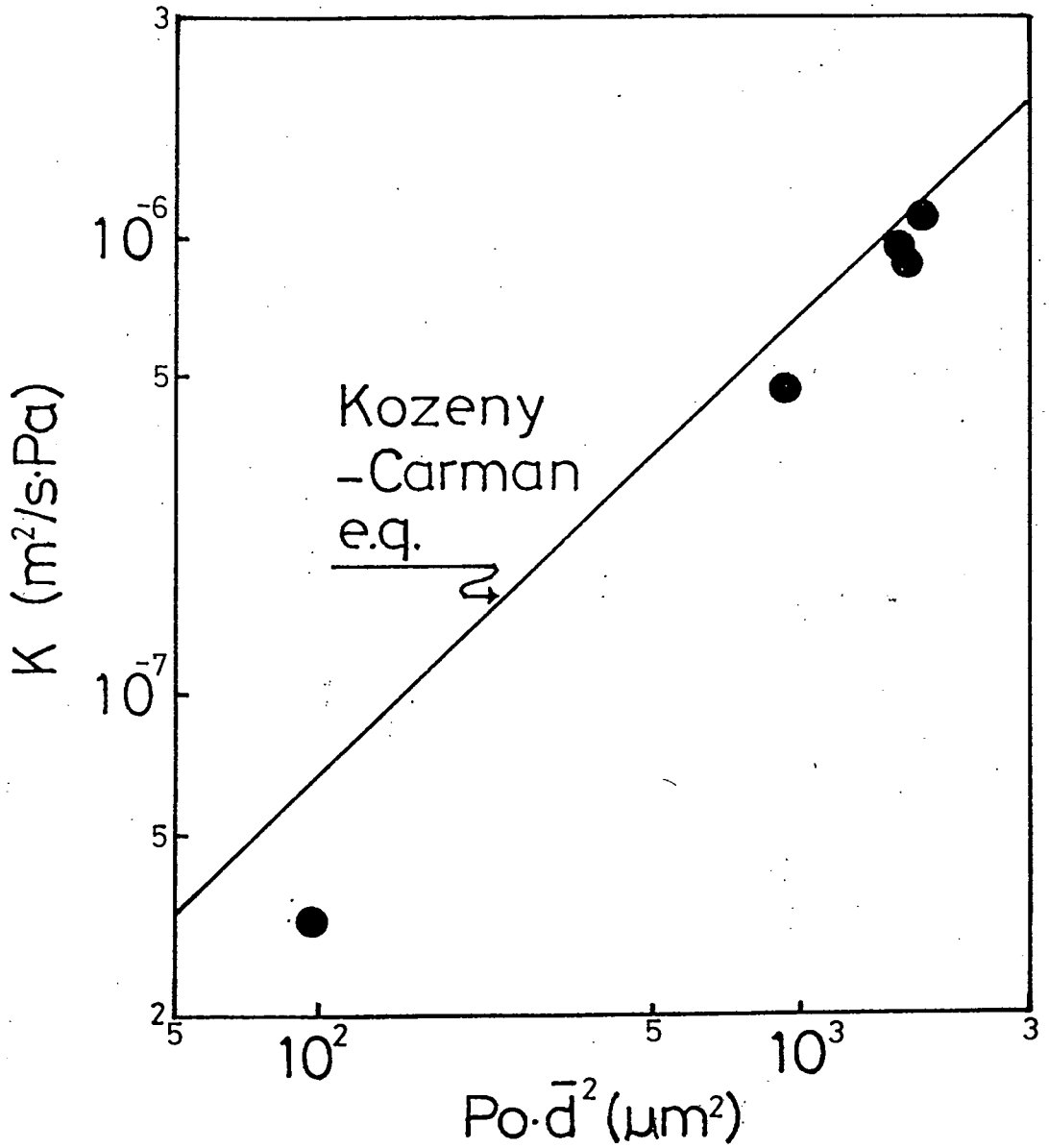

Figure 5.24 Influence of Apparent Porosity (P_o) and Mean Pore Size ($\bar{d}$) on Permeability (K)

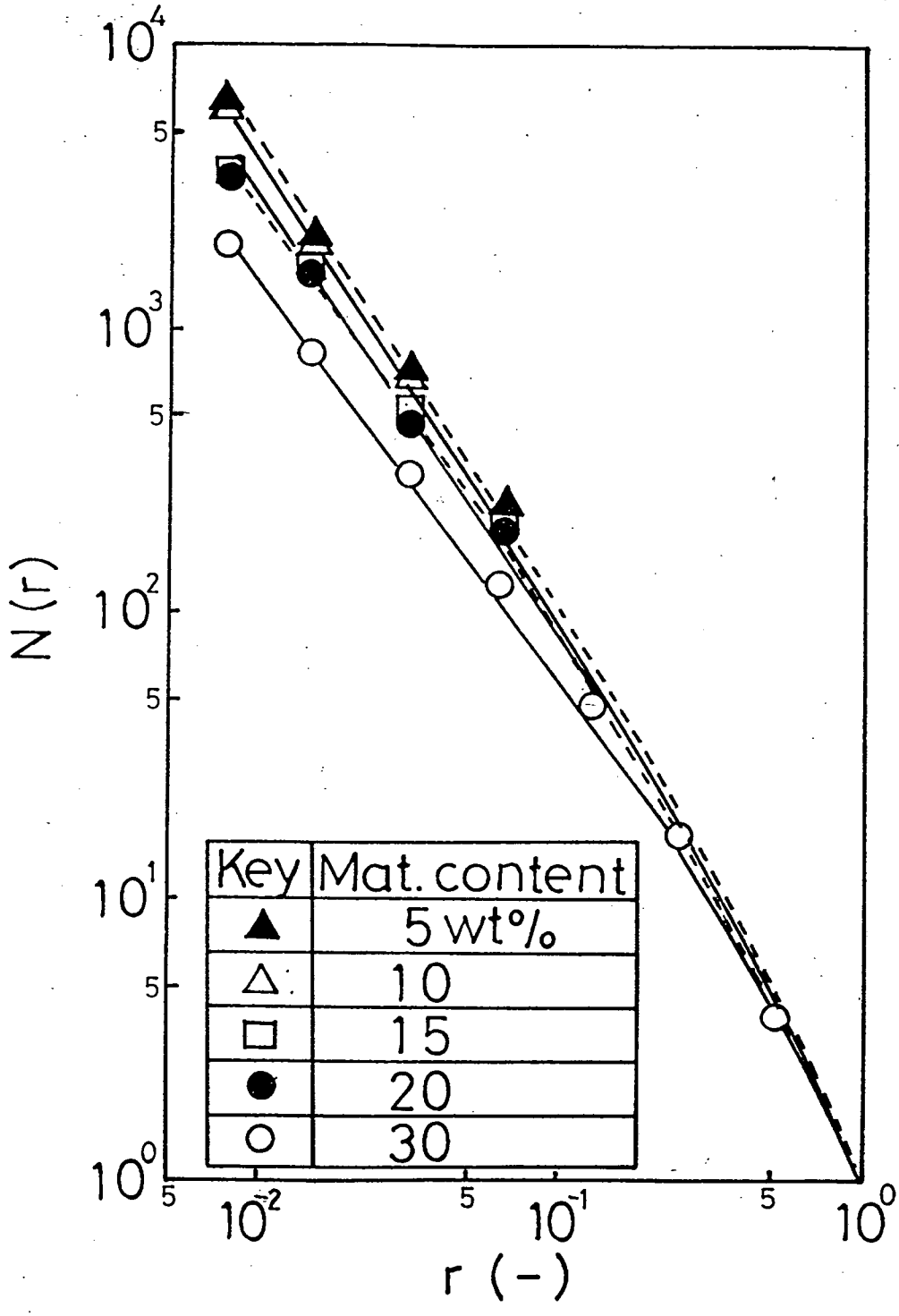

Figure 5.25 Number of Segments N(r) to Cover the Shape of Pores

dimension decreased as the matrix content increased. The lowest fractal dimension of 1.36 for 30 wt. % matrix content was attributed to the existence of more boundary cracks and the penetration of the Ti element and solid solutions into the boundary cracks to yield simpler pore shapes in the TA30 specimen. The fractal dimension dropped sharply at about 10-15 wt. % content, which agreed well with the plot of mean pore size versus permeability in figure 5.24. The relation between fractal dimension and permeability was plotted in figure 5.27. It showed that there was an optimal fractal dimension of 1.57 at which permeability was maximum. The optimal value agreed well with the case of magnesia ceramic (Tsuchinari, A. et.al. 1991). Hence, there existed an effective pore shape that offered minimum gas flow resistance, which characterized the best specimen for refractory work.

In a previous report (Iso, H. et.al. 1985), the firing temperature which caused significant change in pore shape in porous magnesia ceramic was approximately equal to the temperature at which $MgO{\cdot}Al_2O_3$-2 $MgO{\cdot}TiO_2$ solid solution was produced. Therefore, the fractal dimension of pore shape strongly depended on the amount of solid solution. In order to confirm such dependency , the relationship between the fractal dimension and the count per second of the X-ray intensity for $MgO{\cdot}Al_2O_3$ - $2MgO{\cdot}TiO_2$ solid solution was plotted in figure 5.28. Obviously the fractal dimension increased in proportion to the amount of solid solution.

7. Comparison of Physical Properties of $MgO{\cdot}Al_2O_3$ Refractory with MgO Refractory.

The results of previous experiments on MgO refractory (Tsuchinari, A. et.al. 1991) , which was composed of the same matrix powder but different aggregate particles, was compared with this experiment. Bulk density was reported to decrease sharply at low matrix contents and increased gradually at high contents, which showed contradictory tendency against the present experiments. Furthermore, the fractal dimension of the previous refractory increased, but the present one decreased, with the matrix content, although permeability and mean pore size of both refractories had maximum values around at $D = 1.56 \sim 1.57$.

Since the important differences in the composition of both refractories were the amount of MgO in the aggregate particles that

controlled the formation of the solid solution $MgO \cdot Al_2O_3$-$2MgO \cdot TiO_2$, these differences in physical properties could reasonably be attributed to the difference in MgO contents.

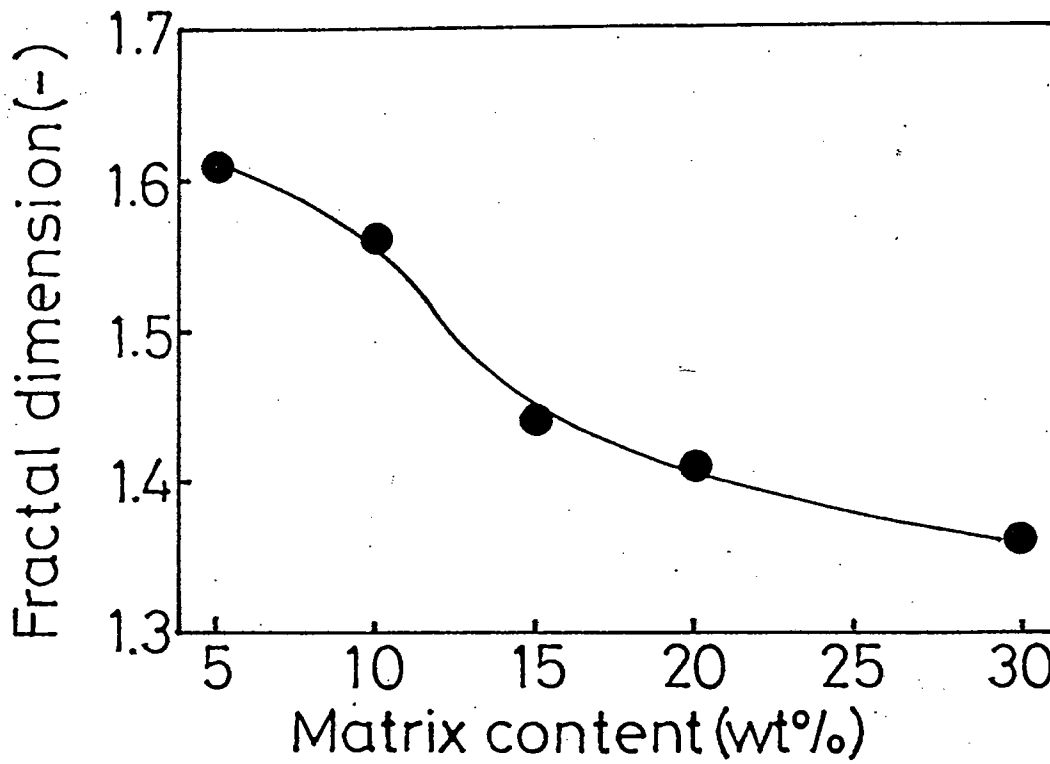

Figure 5.26 Relation between Fractal Dimension and Matrix Content

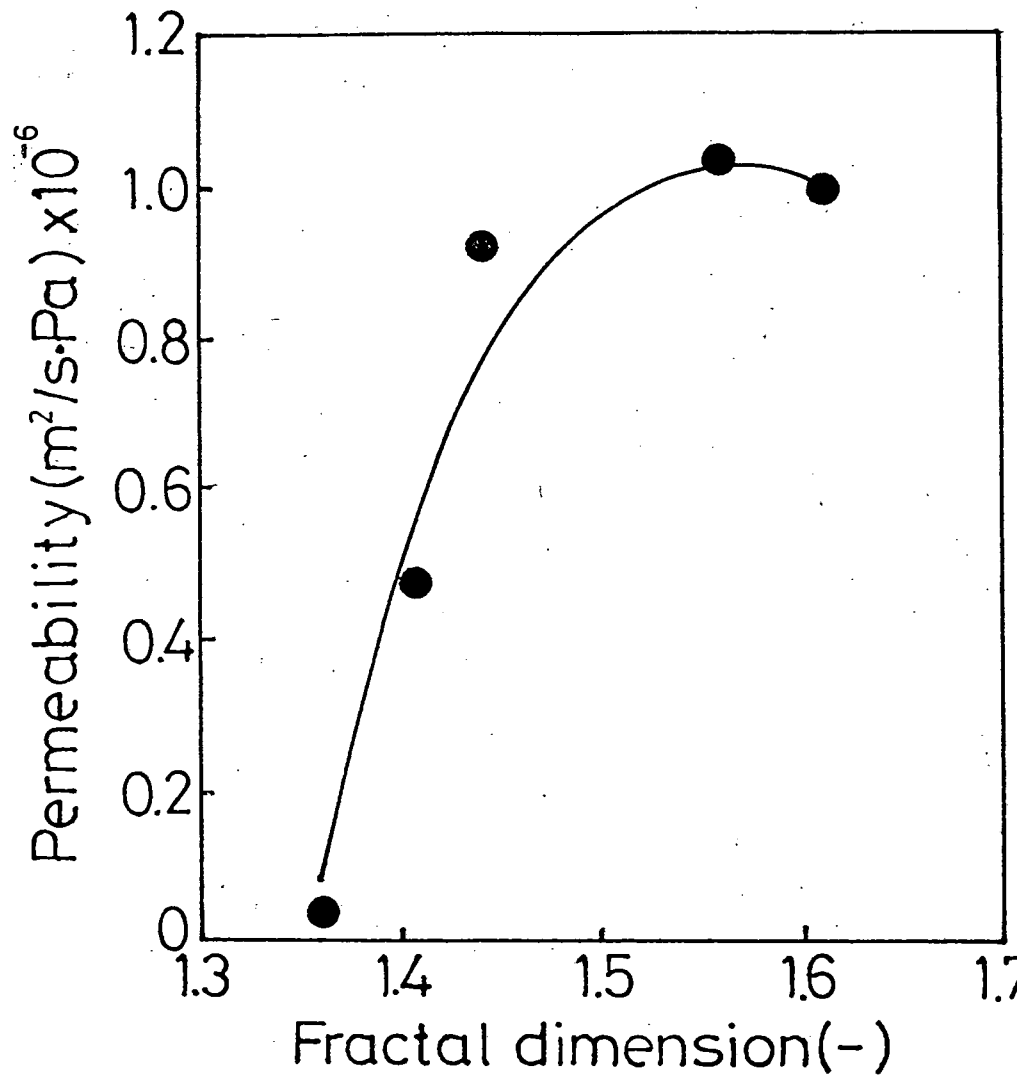

Figure 5.27 Influence of Fractal Dimension on Permeability

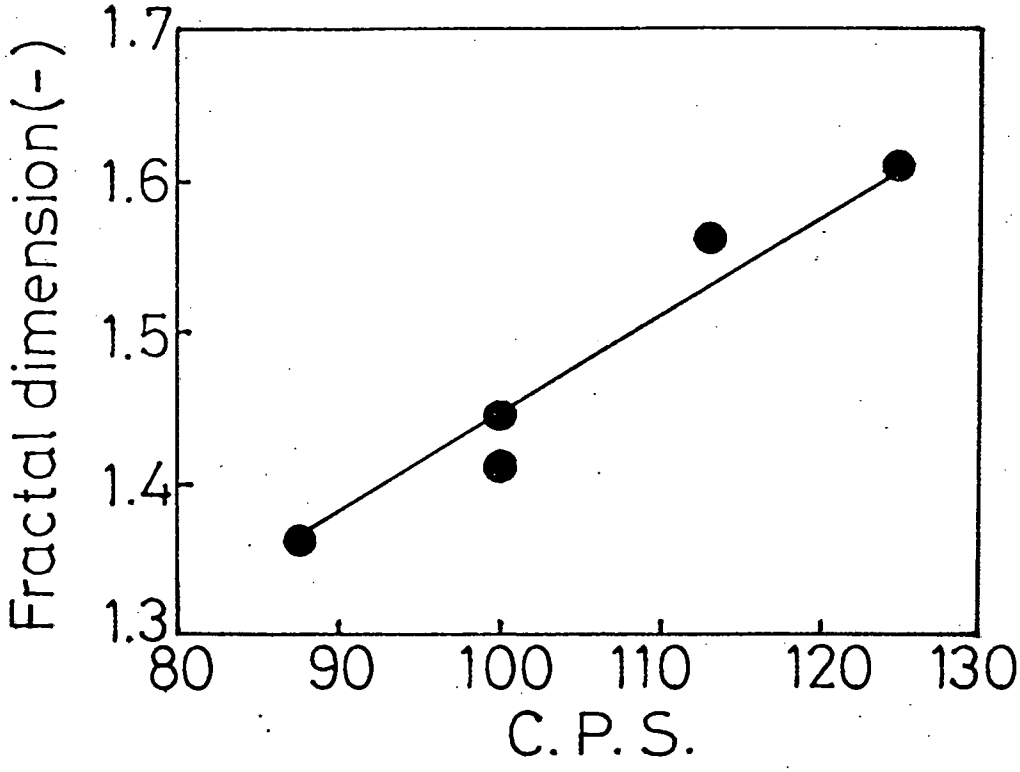

Figure 5.28 Relation between Fractal Dimension and Count per Second of X-ray Intensity for MgO. Al_2O_3-2MgO.TiO_2 s.s.